

1 **An evaluation of kilometer-scale ICON simulations of**
2 **mixed-phase stratocumuli over the Southern Ocean**
3 **during CAPRICORN**

4 **Veeramanikandan Ramadoss¹, Kevin Pfannkuch¹, Alain Protat², Yi Huang^{3,4},**
5 **Steven Siems⁵ and Anna Possner¹**

6 ¹Institute for Atmospheric and Environmental Sciences, Goethe University, Frankfurt, Germany

7 ²Australian Bureau of Meteorology, Melbourne, Victoria, Australia

8 ³The University of Melbourne, School of Geography, Earth and Atmospheric Sciences, Melbourne, VIC,
9 Australia

10 ⁴Australian Research Council Centre of Excellence of Climate Extremes, Melbourne, Australia

11 ⁵Monash University, Melbourne, VIC, Australia

12 **Key Points:**

- 13 • The continuous formation, in-cloud layer growth by riming, and sub-cloud layer melt-
14 ing of graupel are crucial to represent observed Southern Ocean stratocumulus cloud-
15 precipitation structures during CAPRICORN.
- 16 • Boundary layer decoupling is reasonably captured in km-scale simulations when the
17 positive bias in the prescribed ERA5 SST is removed.
- 18 • During CAPRICORN 2016, graupel melting is the predominant rain source in South-
19 ern Ocean stratocumuli as simulated in ICON.

Corresponding author: Veeramanikandan Ramadoss, ramadoss@iau.uni-frankfurt.de

Abstract

This study investigates the representation of stratocumulus (Sc) clouds, cloud variability, and precipitation statistics over the Southern Ocean (SO) to understand the dominant ice processes within the Icosahedral Nonhydrostatic (ICON) model at the kilometer scale using real case simulations. The simulations are evaluated using the shipborne observations as open-cell stratocumuli were continuously observed during two days (26th-27th of March 2016), south of Tasmania. The radar retrievals are used to effectively analyze the forward-simulated radar signatures from Passive and Active Microwave TRAnsfer (PAMTRA). We contrast cloud-precipitation statistics, and microphysical process rates between simulations performed with one-moment (1M) and two-moment (2M) microphysics schemes. We further analyze their sensitivity to primary and secondary ice-phase processes (Hallett–Mossop and collisional breakup). Both processes have previously been shown to improve the ice properties of simulated shallow mixed-phase clouds over the SO in other models. We find that only simulations with continuous formation, growth, and subsequent melting of graupel, and the effective riming of in-cloud rain by graupel, capture the observed cloud-precipitation vertical structure. In particular, the 2M microphysics scheme requires additional tuning for graupel processes in SO stratocumuli. Lowering the assumed graupel density and terminal velocity, in combination with secondary ice processes, enhances graupel formation in 2M microphysics ICON simulations. Overall, all simulations capture the observed intermittency of precipitation irrespective of the microphysics scheme used, and most of them sparsely distribute intense precipitation ($>1 \text{ mm h}^{-1}$) events. Furthermore, the simulated clouds are too reflective as they are optically thick and/or have high cloud cover.

Plain Language Summary

Stratocumulus (Sc) clouds cover a large portion of the Southern Ocean (SO), where they substantially cool the ocean surface. Our understanding of the complex physics of these clouds, which include both liquid and ice remains incomplete, and hence the representation of these clouds in global climate and weather models remains biased. In particular, their timing, frequency of occurrence, cloud phase and distribution, cloud cover, and precipitation characteristics are still associated with open research questions. This results in SO radiative biases and increased uncertainty for estimating climate sensitivity. We use the measurements from the Clouds, Aerosols, Precipitation, Radiation, and atmospheric Composition Over the southern ocean (CAPRICORN) voyage south of Tasmania, to evaluate the representation of broken cloud fields, the dominant ice processes, and the precipitation characteristics in the high-resolution numerical simulations. Our results suggest that, in addition to capturing the observed discrete cloud events, the graupel formation, its growth in the cloud layer, and subsequent melting in the sub-cloud layer are critical processes in accurately representing the SO broken Sc fields and precipitation characteristics during CAPRICORN. Additionally, compared to observations, the simulated clouds are too reflective.

1 Introduction

The Southern Ocean (SO) (45°S-65°S, 180°W-180°E) is one of the regions with the highest annually-averaged low cloud fraction of 60% (Muhlbauer et al., 2014). The low clouds, in particular, stratocumulus (Sc) clouds are capped by a strong temperature inversion of 10-20 K in just a few vertical meters at the top of the Sc topped boundary layer (Riehl et al., 1951; Caughey et al., 1982; Bosello et al., 2007). Cloud-top (CT) radiative cooling due to longwave emission is the most crucial mechanism that drives the convective instability to sustain Sc clouds, and further enhances the inversion at the CT. The supply of moisture from the ocean surface by latent heating, cooling from evaporation and sublimation in the sub-cloud layer (cold pool generation), the associated large-scale turbulent eddies, entrainment from the free tropospheric atmosphere at the CT, and precipitation are the processes interlinked with the mesoscale variability of Sc clouds (Bosello et al., 2007).

Precipitation and albedo strongly depend on the micro- and macrophysical properties, and the spatio-temporal distribution of hydrometeors within the Sc cloud field. A numerical weather or climate model must capture the aggregated effect of all these complex processes which occur at diverse spatial and temporal scales in its grid-scale tendencies and diagnostic variables.

A study by Bodas-Salcedo et al. (2012) with the atmosphere-only Met Office model reported that the low and mid-level clouds at the lee of the cold front of cyclones in the SO are responsible for the downwelling SW positive bias. The representation of Sc clouds largely differs in the 6th Coupled Model Intercomparison Project (CMIP6) compared to CMIP5 (Schuddeboom & McDonald, 2021). The SO Sc clouds were too few and too bright in CMIP5, whereas they occur more often in CMIP6, and are not brighter compared to Clouds and the Earth’s Radiant Energy System (CERES) data. While a correct representation of cloud macrophysics alone is not a sufficient criterion, a better representation of cloud microphysics is essential for addressing the SW bias (Fiddes et al., 2022). The microphysics parameterization controls the shape, size, and concentration of liquid and ice hydrometeors in the SO Sc mixed-phase clouds (MPCs), and which strongly influence the cloud radiative effect.

Many models underestimate the presence of supercooled liquid water (SLW), since ice grows at the expense of liquid water in MPCs when the ambient vapor pressure is subsaturated and supersaturated with respect to liquid and ice respectively (termed as the Wegener-Bergeron-Findeisen process). The deficiency of the models in simulating supercooled liquid in SO MPCs can be compensated by slowing down the vapor deposition growth rate of ice crystals. This can be achieved by modifying the shape parameter of ice crystals. Although the focus is the SO, this has an impact on the liquid water content in either hemisphere (Varma et al., 2020). The ice formation process in mixed-phase Sc clouds is poorly understood (Fridlind et al., 2007), and the ice crystal number concentration (ICNC) is one of the largest uncertainties in these SO clouds. Heterogeneous nucleation requires ice nucleating particles (INPs) for droplet freezing where SLW prevails in metastable equilibrium. Nevertheless, the SO is a remote region with very low INP concentrations. For example, INP concentrations of 0.38 to 4.6 m⁻³ were observed at -20°C during March-April 2016 (McCluskey et al., 2018). The sparse INPs in SO limit droplet freezing and further the production of ice crystals, resulting in reduced precipitation and brighter clouds (Vergara-Temprado et al., 2018). However, a higher ICNC than INP concentration was observed during an earlier SO campaign. This was associated with the secondary ice production processes (Huang et al., 2017). The rime splintering process by Hallett and Mossop (1974), or HM, a predominant secondary ice production process in global climate models, is insufficient to account for the observed ICNC. The deficiency in the modeled ICNC in this remote atmosphere can be better described by HM in conjunction with collisional breakup processes (Sotiropoulou et al., 2020).

The objective of this paper is to investigate the significance of ice processes and the associated precipitation, and to understand the dominant microphysical processes in mixed-phase open-cell stratocumuli using numerical simulations. In this study, we evaluate the kilometer-scale ICON-NWP (Icosahedral Nonhydrostatic – Numerical Weather Prediction) simulations with the shipborne in-situ and remote sensing observations obtained during Clouds, Aerosols, Precipitation, Radiation, and atmospheric Composition Over the southern ocean (CAPRICORN) on 26th-27th of March 2016, south of Tasmania. Among the numerous observations, a suite of instruments measured the cloud and precipitation characteristics, boundary layer structure, and surface energy fluxes during this first voyage of CAPRICORN (Mace & Protat, 2018a, 2018b). A set of convection-permitting simulations (referred to as “kilometer-scale”) are performed in this study. The kilometer-scale simulations with active shallow-convection parameterization are used to address the following research questions in this study.

- 122 • How well do kilometer-scale ICON simulations capture the vertical structure of post-
123 frontal mixed-phase cloud-precipitation in SO?
- 124 • How do different ice-phase processes impact precipitation formation in observed and
125 simulated mesoscale cellular convective (MCC) clouds during CAPRICORN?
- 126 • Are these conclusions robust across different microphysics schemes of varied complex-
127 ity available within ICON?

128 **2 Observations, Simulations, and Analysis Methods**

129 **2.1 Observations**

130 The CAPRICORN voyage I took place south of Tasmania from the 13th of March 2016
131 to the 15th of April 2016. During this time a consistent period of post-frontal open MCC
132 clouds was observed between 26th and 27th of March 2016. The time period is characterized
133 by a high-pressure system of 1030 hPa located south-west of Australia on the 26th of March
134 2016 (Figure 1a). A long cold front that stretches from 38°S-60°S, which is associated with
135 the high-pressure system, passed the ship on 25th of March 2016 and Tasmania on 26th of
136 March 2016. Open MCC clouds were observed for 36 hours at the lee of the cold front 6
137 hours later of its transit, followed by closed MCC clouds later on (Lang et al., 2021). Char-
138 acterizing the clouds and precipitation properties and examining their occurrence statistics
139 were part of the objective of the CAPRICORN field study using modern in-situ and remote
140 sensing instruments aboard the R/V Investigator. A comprehensive overview of all instru-
141 ments is provided in Mace and Protat (2018a, 2018b). Here, we only focus on measurements
142 and retrievals relevant for this study.

143 The thermodynamic profiles of the atmosphere are obtained from radiosondes on 26th
144 of March 2016 at 01:42:00 UTC and 06:24:00 UTC. The intensities of precipitation are ob-
145 served from Ocean Rain and Ice-Phase Precipitation Measurement Network (OceanRAIN)
146 disdrometer (Klepp, 2015). The downwelling SW radiation is measured from Precision
147 Spectral Pyranometer (PSP) at the port and starboard sides of the R/V Investigator.
148 The cloud-precipitation vertical structure is characterized by a 95-GHz single-polarization
149 Bistatic Radar System for Atmospheric Studies (BASTA) Doppler cloud radar with a verti-
150 cal resolution of 25 m and temporal resolution of 12 s (Delanoë et al., 2016). The cloud base
151 phase (CBP) and the cloud base height (CBH) are derived from a 355 nm cloud-aerosol
152 Leosphere RMAN-511 mini-Raman lidar with a vertical resolution of 15 m and temporal
153 resolution of 35 s (Royer et al., 2014). The SST is measured from an in-situ instrument
154 (which was the source of the sea surface temperature (SST) bias - see section 2.2.3) mea-
155 sures. The combined radar and lidar data (termed as the radar-lidar merged product) with
156 a vertical resolution of 25 m and temporal resolution of 1-min is used to determine cloud
157 phase. Temperature from the ERA-interim reanalysis is interpolated onto the pixels of the
158 radar-lidar merged product. At sub-freezing temperatures, each pixel is classified as (a)
159 SLW if only lidar signal is detected, (b) mixed-phase if lidar and radar signals are detected,
160 and (c) mixed-phase or ice-phase if only a radar signal is present (Noh et al., 2019). The
161 layer integrated lidar backscatter and lidar depolarization ratio (δ) are used (see section 2.3
162 for details) to determine CBH and CBP (Hu et al., 2009, 2010; Alexander & Protat, 2018;
163 Mace & Protat, 2018a).

164 **2.2 Simulations**

165 **2.2.1 Model Setup**

166 Real case simulations are performed with ICON-NWP. The initial and hourly lateral
167 boundary conditions are derived from the European Centre for Medium-Range Weather
168 Forecasts fifth reanalysis (ERA5). The dynamical downscaling of ERA5 to the kilometer
169 scale is achieved by a two-way nesting strategy (Figure 1b). Across three domains the
170 horizontal resolution is roughly doubled each time from 4.9 km to 2.4 km to the highest

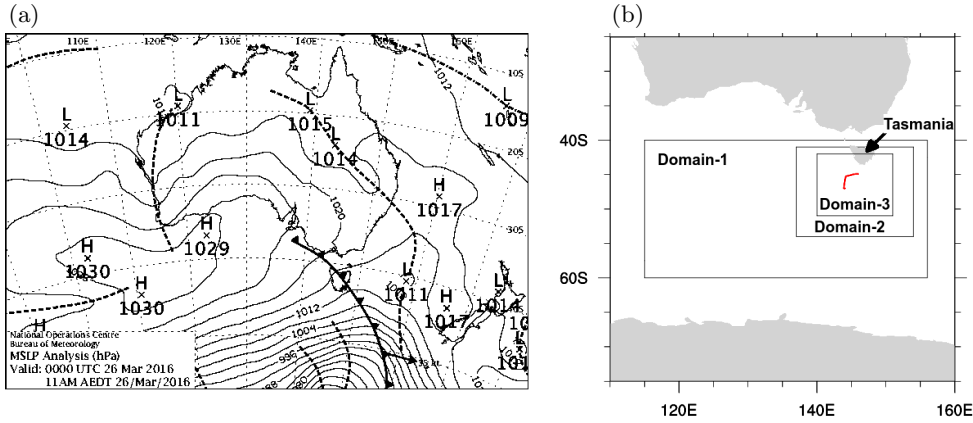


Figure 1: (a) Map of synoptic conditions south of Tasmania on 26th of March 2016 at 00 UTC. (b) ICON nested domains for simulation, where Domain-1 (outer domain) has 264948 cells with 4.9 km of horizontal resolution, Domain-2 has 304100 cells with 2.4 km of resolution, Domain-3 (highest resolution domain) has 556216 cells with 1.2 km of resolution, and the red line shows the ship track for two days (26th-27th of March 2016).

171 resolution of 1.2 km. To minimize the numerical error in this study, the two-day (26th of
 172 March 2016 at 00:00:00 UTC to 28th of March 2016 at 00:00:00 UTC - case study period)
 173 simulation period was split into two 36 h time periods. The first 12 hours of each simulation
 174 are used as spinup. Furthermore, the last 12 hours of the first run (12 UTC of 25th of March
 175 until 00 UTC of 27th of March) overlap with the first 12 hours of the second run (12 UTC of
 176 26th of March until 00 UTC of 28th of March). The model is run with 60 vertical layers and
 177 a model top height of 23 km. The layers within the boundary layer are stretched from 20 to
 178 200 m in thickness. From Mellor and Yamada (1982), the turbulence scheme developed by
 179 Raschendorfer (2001) based on the prognostic turbulent kinetic energy (TKE) equation with
 180 2nd order closure on level 2.5 is used. The rapid radiative transfer model (RRTM) developed
 181 by (Mlawer et al., 1997) is used for radiation. All convection is parameterized following the
 182 approach of Bechtold et al. (2008). In the kilometer-scale resolution domain (1.2 km), only
 183 shallow convection is parameterized. Horizontal cloud variability at the kilometer scale was
 184 best captured in simulations with parameterized shallow convection, which was thus kept
 185 turned on while all other convection parameterizations were turned off. All the runs with
 186 this setup are summarized in Table 1.

187 **2.2.2 Microphysics Sensitivity Experiments**

188 The sensitivity of the simulated cloud precipitation and cloud phase statistics are ex-
 189 plored with respect to two different bulk microphysical schemes. The simpler, and compu-
 190 tationally more efficient, one-moment (1M) scheme (Doms et al., 2011; Seifert, 2008) runs
 191 with fixed assumed number concentrations. Meanwhile a fully prognostic description of
 192 both, number and mass - and thus size-, is used in the two-moment (2M) scheme (Seifert
 193 & Beheng, 2006). The 1M control simulation (1M.90ND) is performed with a cloud droplet
 194 number concentration (CDNC) representative for SO austral conditions. This was deter-
 195 mined as 90 cm⁻³ derived from the combined data of CAPRICORN I, II, and MARCUS
 196 (Measurements of Aerosols, Radiation, and Clouds over the Southern Ocean) for the aus-
 197 tral summer months of November-April (Mace, Protat, et al., 2020). The sensitivity with
 198 respect to prescribed CDNC is investigated in an additional run with a lower prescribed
 199 CDNC of 20 cm⁻³ (1M.20ND), which is representative for austral autumn observations ob-
 200 tained during CAPRICORN I (Mace, Benson, & Hu, 2020) and austral winter aircraft ob-
 201 servations (Ahn et al., 2017). In the 1M microphysics scheme, the ICNC is diagnosed using
 202 the temperature-dependent Cooper parameterization (Cooper, 1986), where heterogeneous
 203 ice nucleation occurs below a temperature threshold of -5°C.

Expt No.	Expt Name	Equation/Description
Bulk microphysics sensitivity experiments (Simulation period: 48 hours)		
1	1M.20ND	1M microphysics scheme and CDNC = 20 cm^{-3}
2	1M.90ND (control simulation)	1M microphysics scheme and CDNC = 90 cm^{-3}
3	2M.P	2M microphysics scheme and no secondary ice-phase processes
4	2M.HM	2M microphysics scheme with rime splintering secondary ice process
5	2M.HM.BR03	2M microphysics scheme with rime splintering and collisional breakup (rimed mass fraction is 0.3) secondary ice process
Microphysical process sensitivity experiments (Simulation period: 24 hours)		
1	2M.HM	Default: CCN = 400 cm^{-3} ; power-law for $v_r = 95.5616 * \exp(0.22 * \log(x_r))$; Ice to snow minimum diameter threshold = $100 \mu\text{m}$; low graupel density; low graupel velocity; graupel maximum diameter (= 2 mm); $v_i = 27.7 * \exp(0.21579 * \log(x_i))$
2	2M.P	Secondary ice production processes switched off
3	2M.HM.BR03	Collisional breakup with rimed mass fraction = 0.3
4	CCN10	CCN = 10 cm^{-3}
5	CCN1000	CCN = 1000 cm^{-3}
6	aukcc*0.5	Autoconversion cloud kernel coefficient is reduced by 50% (= $0.5*6E2$)
7	aukcc*2	Autoconversion cloud kernel coefficient is doubled (= $2.0*6E2$)
8	ice_vel_coef	$v_i = 317 * \exp(0.363 * \log(x_i))$
9	rain_atlas	$v_r = 9.292 - (9.623 * \exp(-622.2 * a_{\text{geo}} * \exp(b_{\text{geo}} * \log(x_r))))$
10	agg_50	Aggregated ice to snow minimum diameter threshold = $50 \mu\text{m}$
11	agg_200	Aggregated ice to snow minimum diameter threshold = $200 \mu\text{m}$
12	gr_d_m	$d_g = 0.3456 * x_g^{0.3571}$ (Medium lump graupel density)
13	gr_d_h	$d_g = 0.3456 * x_g^{0.3704}$ (High lump graupel density)
14	gr_v_h	$v_g = 9.4465 * x_g^{0.12}$ (High lump graupel velocity)
15	gr_max_dia	Graupel maximum diameter increased to 5 mm

Table 1: Bulk microphysics sensitivity experiments for the entire simulation period (26th of March 2016 at 00:00:00 UTC to 28th of March 2016 at 00:00:00 UTC) and microphysical process sensitivity experiments with 2M microphysics scheme (simulated on 27th of March 2016). v , terminal velocity of hydrometeors in $m s^{-1}$; d , diameter of hydrometeors in m ; x , mass of hydrometeors in kg ; $v_{\text{sed},i}$ is maximum sedimentation velocity of ice; CCN, cloud condensation nuclei; CDNC, cloud droplet number concentration; a_{geo} and b_{geo} constants in rain hydrometeor mass - fall speed relation; subscripts r , i and g represent rain, ice and graupel respectively.

204 To better understand the significance of ice processes in SO mixed-phase Sc clouds, sensi-
205 tivity experiments were carried out with the 2M scheme since it has control over CCN and
206 INP specifications. The cloud-precipitation vertical structure and the precipitation statistics
207 as the result of cloud ice processes are studied using sensitivity experiments: 2M.P, 2M.HM,
208 and 2M.HM.BR03 described in Table 1. The collisional breakup parameterization developed

209 by Phillips, Yano, and Khain (2017); Phillips, Yano, Formenton, et al. (2017) based on the
 210 principle of ejected fragments as a function of the initial collisional kinetic energy of solid
 211 hydrometeors is implemented for ice, snow and graupel in ICON. The parameterization of
 212 prognostic CDNC is adapted from Segal and Khain (2006) and the prognostic ICNC from
 213 Seifert and Beheng (2006). The activation scheme for CDNC is computed for a prescribed
 214 lognormal aerosol size distribution with a mean number concentration of 400 cm^{-3} and a
 215 mean radius of $0.04\ \mu\text{m}$ (see supporting information S2). Immersion freezing for sea spray
 216 aerosols is parameterized by McCluskey et al. (2018) and dust aerosol by Demott et al.
 217 (2015); McCluskey et al. (2019). These adjustments to the default heterogeneous freezing
 218 parameterization Seifert and Beheng (2006) were performed to better capture the remote
 219 aerosol environment of the SO relevant for INP nucleation. A fictitious increase of the po-
 220 tential INPs at low temperatures was avoided by relaxing INP concentrations exponentially
 221 with height over 4 km. Immersion freezing rates are limited to temperatures at or below
 222 -5°C . A small perturbed physical parameter ensemble is performed for 2M simulations for a
 223 range of parameters related to the simulated graupel budget (G_budget) in SO stratocumuli.
 224 In addition to dynamics, the formation and depletion of graupel is based on the sensitivity
 225 of the interlinked microphysical processes. The impact of various factors that can influence
 226 these microphysical processes and further the G_budget is analyzed (microphysical process
 227 sensitivity experiments in Table 1).

228 **2.2.3 SST Bias Correction**

229 During CAPRICORN, the instruments for measuring SST were at the ship deck from
 230 22th-26th of March 2016. This biased the assimilation of SST in ERA-Interim, ERA5, and
 231 MERRA-2 products by upto 6°C (Lang et al., 2021). This artificially increases the sea-air
 232 temperature differences, which may have an impact on surface cold pools, boundary layer
 233 decoupling, and the average inversion height. Hence, we corrected the bias by limiting the
 234 maximum SST to 12°C in the entire simulation domain (Figure S1a). We thus ran the
 235 simulations essentially with prescribed SST of 12°C along the track. This fix improved the
 236 overall match between observed and simulated SST and surface fluxes shown in Fig S1, but
 237 fails to capture the $1\text{-}2^\circ\text{C}$ increase in SST after 36 hours which coincides with the transition
 238 of sampling open-cell cloud structures to solid cloud decks towards the end of the 48 hours
 239 period (Figure 2a).

240 **2.3 Analysis Methods**

241 Minimum thresholds are applied in the simulations for all hydrometeor categories.
 242 These are specified as 0.01 g m^{-3} for cloud liquid, 0.0001 g m^{-3} for cloud ice, and 0.00001 g m^{-3}
 243 for rain, snow, graupel, and hail. The simulated cloud-top height (CTH), cloud-top phase
 244 (CTP), CBH and CBP are identified based on these thresholds. Two-dimensional field
 245 statistics are computed in a clipped zone ($147^\circ \geq \text{lon} \geq 143^\circ$; $-44^\circ \geq \text{lat} \geq -48^\circ$) enclosing
 246 the ship track. The retrieved CTH along the ship track has been derived from the ground-
 247 based BASTA radar reflectivity profile. Lidar backscatter is very sensitive to the water
 248 droplet population and attenuates completely within a few tens of meters of the cloud. It is
 249 thus a reliable measure for identifying the CBH. We cannot use the minimum height of the
 250 first backscatter signal of the lidar to determine the cloud base (CB), as this metric may
 251 be biased low by precipitation. Instead, the CBH is calculated as the altitude at which the
 252 maximum vertical gradient of backscatter occurs. The phase partitioning at the CBH is
 253 based on the threshold values for δ (ratio of perpendicular to parallel backscatter intensities
 254 with respect to the transmitter polarization axis). The depolarization ratio is very small for
 255 cloud water and smaller raindrops since the parallel backscatter predominates. Mace and
 256 Protat (2018a) suggest $\delta \leq 0.02$ for liquid-dominant layers and $\delta \geq 0.03$ for ice-dominant
 257 layers. We assumed a mixed-phase category in the in-between range. Since lidar backscatter
 258 is influenced by densely populated hydrometeors in the resolution volume, we are more
 259 likely to miss the presence of ice at CB. Hence we include an additional criterion one level

260 below the identified CB to correct the CBP as ice-phase if $\delta \geq 0.03$ and the temperature is
 261 less than 3°C . The CB precipitation is calculated as the average precipitation in the lowest
 262 one-third of the cloud depth as defined by Wood (2005).

We analyze the microphysical processes with 1M and 2M microphysics schemes to examine the shortcomings in representing the cloud-precipitation vertical structure. The microphysical processes are normalized by the total water vapor loss to the ice-phase (Equation 1) to understand their relative importance, as shown in Equation 2.

$$WVL^*(n, k, i) = X_{nuc}^*(n, k, i) + X_{I_dep}^*(n, k, i) + X_{S_dep}^*(n, k, i) + X_{G_dep}^*(n, k, i) + X_{H_dep}^*(n, k, i) \quad (1)$$

$$\bar{X}(n, k, i) = \frac{\sum_{n,k,i}^{t,4km,nclip} X^*(n, k, i) V(n, k, i)}{\sum_{n,k,i}^{t,4km,nclip} WVL^*(n, k, i) V(n, k, i)} \quad (2)$$

263 Here, V is the cell volume (m^3); WVL^* is the total water vapor loss to the ice-phase (kg m^{-3}
 264 s^{-1}); X^* is the rate of the mass density for a given microphysical process ($\text{kg m}^{-3} \text{s}^{-1}$); X_{nuc}^* ,
 265 X_{idep}^* , X_{sdep}^* , X_{gdep}^* , X_{hdep}^* are the rate of mass density of ice nucleation, ice deposition,
 266 snow deposition, graupel deposition and hail deposition ($\text{kg m}^{-3} \text{s}^{-1}$) respectively; $\bar{X}(i,j,k)$ is
 267 calculated for a time period t (index n), up to 4 km altitude (index k) and the spatial extent
 268 (index i) is clipped around the ship track (nclip: $147^\circ \geq lon \geq 143^\circ$; $-44^\circ \geq lat \geq -48^\circ$).

269 Furthermore, the forward simulated ICON output from the Passive and Active Mi-
 270 crowave TRAnsfer (PAMTRA) model (Mech et al., 2020) is evaluated against the BASTA
 271 radar retrievals. For evaluating the simulation with CAPRICORN, the mean of the sim-
 272 ulated data within 2 km at each coordinate along the ship track is used. The supporting
 273 information S1 provides a basic setup of PAMTRA for 1M and 2M simulations.

274 3 Results

275 Cloud and precipitation characteristics during CAPRICORN between the 26th and 27th
 276 of March 2016 have been studied in great detail in Lang et al. (2021). They hypothesized
 277 that ice processes could play a significant role in the SO open-cell precipitation during this
 278 period. In this section, we use the retrieved cloud properties and precipitation characteristics
 279 from the observations to evaluate the skill of kilometer-scale ICON simulations (control
 280 simulation). Collected soundings (Figures S2a and S2b) are compared to the simulated
 281 soundings in the post-frontal environment of the control simulation (1M.90Nd). Note, that
 282 the second sounding is the thermodynamic profile obtained during the open-cell period.
 283 While the overall profiles are well captured, the inversion height is underestimated by at
 284 least 200 m during the open-cell period (Figure S2b). The transition layer that separates
 285 the two observed cloud layers is located at 1.2 km (0.9 km), and 1.7 km (1.8 km) in the
 286 first and second observed (simulated) sounding respectively. Although the simulated CTH
 287 is underestimated in the second profile, the simulated mean CTH along the ship track is
 288 slightly overestimated at 2.2 km as compared to the observed 1.8 km.

289 3.1 Evaluation of Cloud-Precipitation Vertical Structure and Statistics

290 The vertically pointing single-polarization Doppler radar reflectivity is used to evaluate
 291 the vertical cloud and precipitation structures. Figure 2a shows that intermittent radar
 292 reflectivities occur throughout the two days characterizing sporadic precipitation events.

293 The increase in reflectivity across the melting layer is caused by the higher reflectivity of
 294 liquid hydrometeors than previously frozen hydrometeors (i.e. cloud ice, snow and graupel).
 295 The melting of solid hydrometeors produces liquid precipitation of reduced size, which is
 296 characterized by a higher terminal fall velocity than ice particles due to an increase in
 297 density. This is clearly visible in the more negative Doppler velocities below the melting
 298 layer (Figure S3a). Furthermore, this decrease in Doppler velocity across the melting layer is
 299 well captured by the simulations. However, the mean Doppler velocity of melted rain seems
 300 biased low (falling faster) in 1M.90ND. Furthermore, the presence of ice above the freezing
 301 line is further supported by the merged radar-lidar product (Figure 2c). Most streaks (also
 302 termed as cloud events) above the melting level are classified as mixed-phase, or consist of
 303 adjacent patches of ice and SLW.

304 To understand the formation and evolution of precipitation in the cloud and the cloud-
 305 precipitation vertical structure, we generate (Figure 2a) a contoured frequency by altitude
 306 diagram (CFAD) from the BASTA radar reflectivity retrieval. The CFAD is normalized by
 307 the total samples in every reflectivity bin. The numbers at the top of the CFAD denote
 308 the number of samples within a reflectivity bin (summed along all altitudes) normalised by
 309 the maximum number of samples (summed across all altitudes) in one reflectivity bin found
 310 across all reflectivity bins. The CFAD aggregates the cloud-precipitation data of the same
 311 reflectivity-height bins across multiple timestamps. Thus a physical relationship between
 312 bins across heights may no longer be given. However, a statistical analysis of all observed
 313 vertical reflectivity profiles (Figures S4a) which exclude “single data” points (“single data”
 314 here refers to the presence of just one single, isolated data point within the column) shows
 315 that, overall 14.7% of all streaks exceed 0 dBZ in the lowest 0.4 km (white box in Figure
 316 S4b). Furthermore nearly all points within this region originated from higher layers and
 317 follow a trajectory of increasing reflectivity with decreasing height (negative inclination).
 318 Similarly 20.8% of all streaks reach low reflectivities of -25 dBZ below 1.2 km. This time a
 319 positive inclination can be observed backtracking these points where reflectivities increase
 320 with altitude. Thus, in this case, the CFAD provides a mean representation of the aggregated
 321 vertical evolution of precipitation.

322 We hypothesize that the negative inclination (0 to 20 dBZ; <1.2 km) in Figure 2e refers
 323 to the melting of solid hydrometeors, enhanced melting of graupel, growth of raindrops by
 324 selfcollection (collision-coalescence), and larger ice hydrometeors coated with the layer of
 325 liquid water. However, the melting of small ice crystals doesn’t cause significant changes in
 326 radar reflectivity and thus cannot contribute to the negative inclination in the CFAD. Pro-
 327 cesses involving the growth of graupel particles (riming, deposition, and collisional growth)
 328 are unlikely to contribute to the downward slope as virtually no solid surface precipitation
 329 was observed during CAPRICORN.

330 Between the positive and negative inclined slopes, the in-cloud layer hydrometeors
 331 are visible along a zero-slope bridge structure (-20 to 10 dBZ between 1.2 and 1.6 km).
 332 The continuous cloud-precipitation events that pass through the bins within -35 dBZ to -
 333 25 dBZ, and 0.4 km to 1.2 km, account for 17.3% of the total timestamps (Figures S4e,f).
 334 Furthermore, most of these events begin above 1.2 km and disappear before reaching 0.4 km.
 335 This is in good agreement with the physical hypothesis presented for the positive inclination,
 336 which is likely driven by the partial evaporation or sublimation of sedimenting rain or ice.
 337 Fall streaks disappearing between 1.2 km and 0.4 km then correspond to precipitation events
 338 which fully sublimated or evaporated before reaching the surface.

339 This arc structure which characterizes the dominant evolution of precipitation observed
 340 during CAPRICORN is well pronounced in the control simulation (Figure 2f). However, the
 341 link (from -5 to 0 dBZ; 1.2 to 1.6 km altitude) between the bridge (here, simulated bridge
 342 refers the bright band from -25 to 0 dBZ; 1.6 to 2 km altitude) and the downward slope
 343 band is poorly represented. This bias is likely caused by the absence of a melting scheme
 344 within PAMTRA and the low vertical resolution of the model output. From the negative
 345 inclination of the arc (reflectivity band between 0 and 20 dBZ), the cloud-precipitation

346 streaks from the bridge firmly reduce to 24%, 11% and 9% below 1.2 km towards near-
 347 surface, whereas 25%, 24% and 26% were observed during CAPRICORN. The decreasing
 348 percentage is either related to a steady decline in raindrop size due to evaporation if the
 349 downward change in reflectivity of the streaks is negative, or an increase in raindrop size
 350 due to collision-coalescence if the downward change in reflectivity is positive. Meanwhile,
 351 percentage increases are associated with an abrupt loss in raindrop size as the reflectivity
 352 streaks pass through the multiple reflectivity bins inside the height bins less than 0.4 km.
 353 This may result in larger raindrops in the control simulation as their evaporation is more
 354 effective at altitudes below 0.4 km in CAPRICORN. To better understand the origin of the
 355 bridge structure, the contribution of each hydrometeor species was analyzed individually.
 356 This was done to get a sense of the relative importance between the individual hydrometeor
 357 species. However, one cannot expect the individual contributions listed in Table S1 to
 358 be additive. We find that graupel hydrometeors alone contribute 66% to the total bridge
 359 reflectivity structure in the control simulation. Thus in ICON, precipitation statistics are
 360 largely influenced by the in-cloud formation and sub-cloud layer evolution of graupel.

361 Here, we compare the simulated statistics and variability of precipitation between obser-
 362 vations and simulations across a single track observed from the ship over a two-day period.
 363 Thus, it is unlikely that these single track measurements capture the entire variability of
 364 the low cloud-precipitation system. To account for that, we generate a small ensemble of
 365 theoretical tracks in the simulations to compare against the observations. In addition to the
 366 ship route, 10 additional tracks are constructed with a 0.2 degree offset (Figure S5). This
 367 yields a total of 11 tracks across which the simulated statistics from point measurements are
 368 compared with the observations. The normalized CFAD considering the full track ensemble
 369 (Figure S6) for the control simulation qualitatively agrees with its same simulation (Figure
 370 2f) just one versus 11 tracks. An average decline in mean bridge reflectivity over all tracks of
 371 10.2% was simulated. This indicates that the single-track observations over this time period
 372 are sufficiently long to characterize the variability of spatio-temporal intermittent vertical
 373 precipitation structures.

374 Figure 2d shows that the simulated cloud phase (see section 2.3 for the definition)
 375 along the ship track qualitatively agrees with the phase distinction of the merged radar-
 376 lidar product (Figure 2c). Furthermore, the simulated MPCs are enriched with graupel. It
 377 is evident that all of the graupel particles (hatching in Figure 2d) melt near the melting level.
 378 In general, radar reflectivity increases towards the ocean surface by collision-coalescence that
 379 efficiently occurs on larger raindrops. The larger raindrops are more likely to occur either due
 380 to the high ambient relative humidity at low levels that reduces the homogenization of the
 381 rain drop size spectrum through evaporation. Additionally, weaker updrafts in comparison
 382 with the raindrop fall velocity (weaker convection) can contribute to this effect as the vertical
 383 segregation by rain drop sedimentation speed is amplified. Most of the simulated surface
 384 precipitation timestamps in the ship track exhibit this phenomenon along the reflectivity
 385 streaks. Additionally, the mean Doppler velocity (MDV) also shows the growth in raindrop
 386 size driven by collision-coalescence (Figure S3b). For example, the precipitation rate of
 387 5.6 mm h^{-1} immediately after the 24th hour (Figure 3b) has an increase in reflectivity of
 388 $>20 \text{ dBZ}$ (Figure 2b) near the ocean surface. Similarly, the MDV decreases to -3.5 m s^{-1}
 389 below the melting level but slightly increases to -3.3 m s^{-1} below 0.4 km. This may be due to
 390 the partial evaporation of the raindrops near the ocean surface. The subcloud evaporative
 391 cooling from precipitation reduces the near-surface air temperature and increases the relative
 392 humidity. The decrease in near-surface air temperature is connected with the emergence of a
 393 surface cold pool, which is a significant criterion for boundary layer decoupling. Further, this
 394 increases the surface SHF and decreases the surface LHF. Increased SHF and decreased LHF
 395 are driven by the increase in the difference between the near-surface air temperature and SST
 396 for the former and increased RH for the latter. These processes were well observed during
 397 CAPRICORN (Lang et al., 2021), and across many timestamps in the control simulation
 398 (Figure 3a).

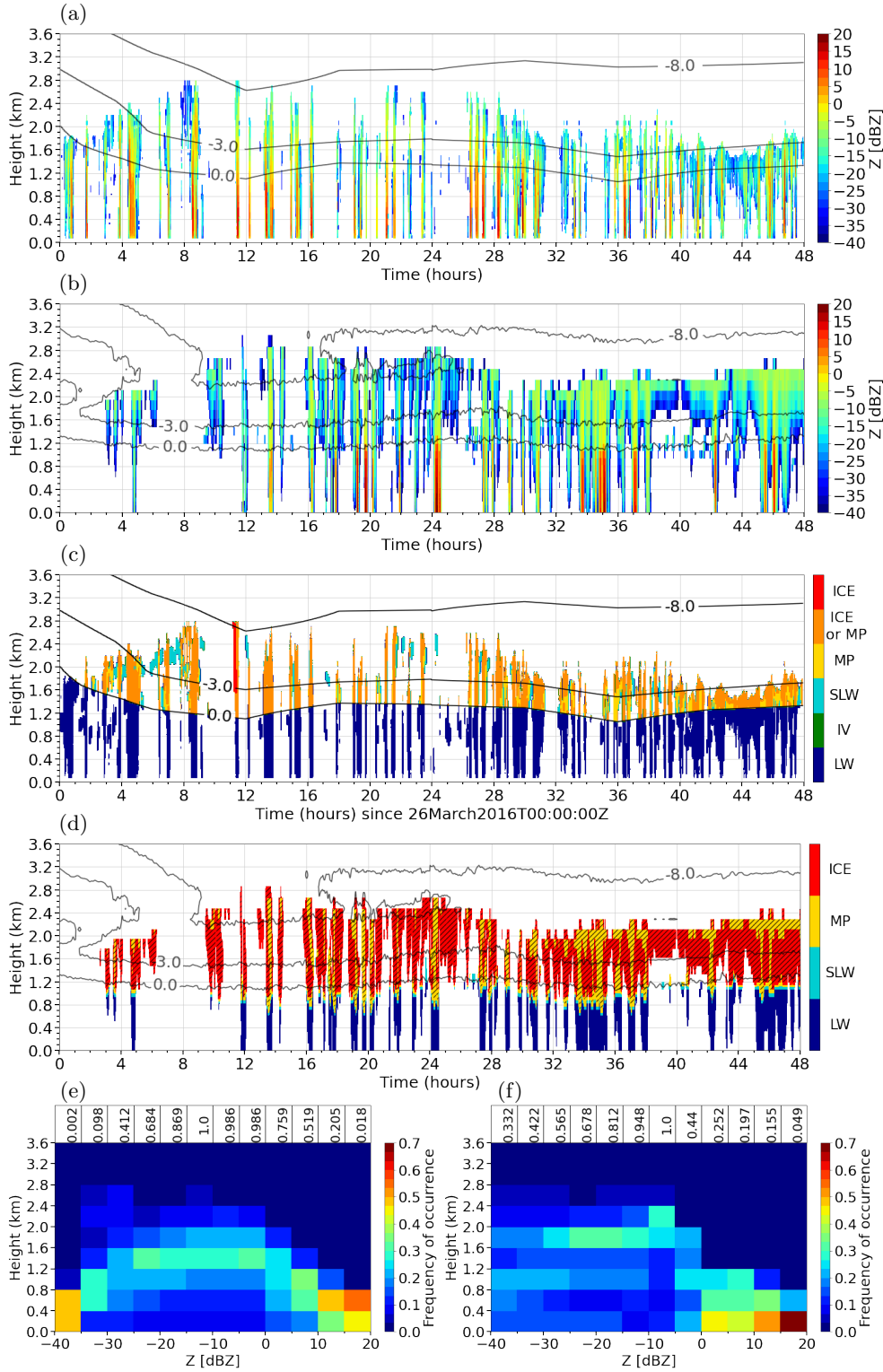


Figure 2: Time-height cross-section with 1-min temporal resolution of (a) BASTA radar reflectivity, (b) simulated radar reflectivity, (c) observed radar-lidar merged cloud-precipitation phase and (d) simulated cloud-precipitation phase. Isotherms in $^{\circ}\text{C}$ (black lines). Normalized contoured frequency by altitude diagrams (CFAD) with 1-min resolution for the case study period of (e) observed radar reflectivity and (f) simulated reflectivity. Simulated data corresponds to control simulation. Case study period: 26th of March 2016 at 00:00:00 UTC to 28th of March 2016 at 00:00:00 UTC. IV, ice virga; MP, mixed-phase; LW, warm liquid water.

399 Among the total cloud-precipitation occurrence fraction of 71.1% along the ship track
 400 for 1M.90ND, 3.6% occurs within the first 6 hours (succeeded by closed to open cells transi-
 401 tion or advection) and 24.8% occurs in the final 12 hours of the simulation period. Similarly,
 402 among the total cloud-precipitation occurrence fraction of 52.4% observed during CAPRI-
 403 CORN, 6.4% occurs within the first 6 hours and 19.5% occurs in the final 12 hours of the
 404 simulation period. This negative bias in the initial period and the positive bias in the final
 405 period for the cloud-precipitation occurrence fraction may be the result of the SST bias
 406 correction. A positively biased SST can cause excessive deepening of the boundary layer
 407 by overestimating the entrainment of free tropospheric dry air, which can cause the under-
 408 estimation of the low-cloud fraction (Bretherton & Wyant, 1997; Sandu & Stevens, 2011;
 409 Lang et al., 2021). The initialized SST is positively biased during the first 6 hours of the
 410 simulation period and negatively biased during the final 12 hours (Figure S1a), explaining
 411 why the simulated occurrence fraction or cloud development was lower for the former and
 412 higher for the latter.

413 Figure 3b shows that low precipitation rates are observed during CAPRICORN and
 414 1M.90ND until the onset of open-cell MCC (open-cell period: 06 to 42 hours). Further-
 415 more, the total accumulated precipitation is realistic at the end of the two days (Figure
 416 3c). Precipitation hardly occurs in the control simulation until 19 hours, whereas frequent
 417 precipitation events are observed during this period in the open-cell region. The mean (95th
 418 percentile) precipitation rate of CAPRICORN and the control simulation are 0.046 mm h^{-1}
 419 (0.05 mm h^{-1}) and 0.051 mm h^{-1} (0.13 mm h^{-1}) respectively. In addition, the occurrence of
 420 only few of these events can drastically alter the accumulated precipitation as seen after
 421 20 and 24 hours. Although the timing of 1M.90ND precipitation rates doesn't agree well
 422 with the observations along the ship track, the interquartile range of quasi-ensemble accu-
 423 mulated precipitation shows an outstanding agreement with the observations (Figure 6b).
 424 The control simulation is skewed to the right (Figure S7), which shows that the stronger
 425 precipitation events ($>1 \text{ mm h}^{-1}$) are sparsely distributed with a mean frequency of occur-
 426 rence of 3.17 as compared to CAPRICORN with 3.67. Furthermore, the variability of the
 427 accumulated precipitation increases considerably in the the southeast of the CAPRICORN
 428 track, while it differs modestly for most of the tracks in the northwest region (Figure S7
 429 and Table S2).

430 The time series of surface precipitation is well aligned with the radar reflectivity pro-
 431 files in both observation and 1M.90ND. Thus we can combine both measurements to learn
 432 more about near-surface precipitation characteristics. By correlating the radar reflectivities
 433 at 75 m altitude (where ground BASTA radar first detected the signal) and the observed
 434 surface precipitation, the minimum reflectivity associated with at least 1 mm h^{-1} of surface
 435 precipitation is 1 dBZ. However, 52.6% of surface precipitation rates lower than 1 mm h^{-1}
 436 are associated with reflectivities larger than 1 dBZ. Using the PAMTRA reflectivities for
 437 1M.90ND and the surface precipitation rates, 1 mm h^{-1} are associated with a considerably
 438 larger minimum reflectivity of 10.8 dBZ. However, only 38.2% of lower precipitation rates
 439 are associated with higher reflectivities. Similarly, for precipitation rates of at least 1 mm h^{-1}
 440 to occur, a maximum criteria of -1.96 m s^{-1} (-2.86 m s^{-1}) MDV is identified for CAPRICORN
 441 (1M.90ND). Yet, 71.4% (24.5%) of lower precipitation rates fall below this criteria. As a
 442 result, the minimum reflectivity (maximum MDV) criteria during the occurrence of sur-
 443 face precipitation above 1 mm h^{-1} with respect to minimum reflectivity (maximum MDV)
 444 is positively (negatively) biased for the control simulation. Furthermore, the number of
 445 events having precipitation rates below 1 mm h^{-1} with respect to the minimum reflectivity
 446 and maximum MDV is negatively biased for the control simulation (Figure S3b). Since
 447 reflectivity is proportional to the sixth power of the size of hydrometeors of similar phase
 448 and MDV decreases with an increase in the size of hydrometeors, this reveals that the con-
 449 trol simulation generates larger near-surface raindrops. This explains why the near-surface
 450 relative occurrence frequency over 10 dBZ in the simulation is higher than observed (Figures
 451 2e and 2f). However, it is important to keep in mind that the Doppler radar was not on a

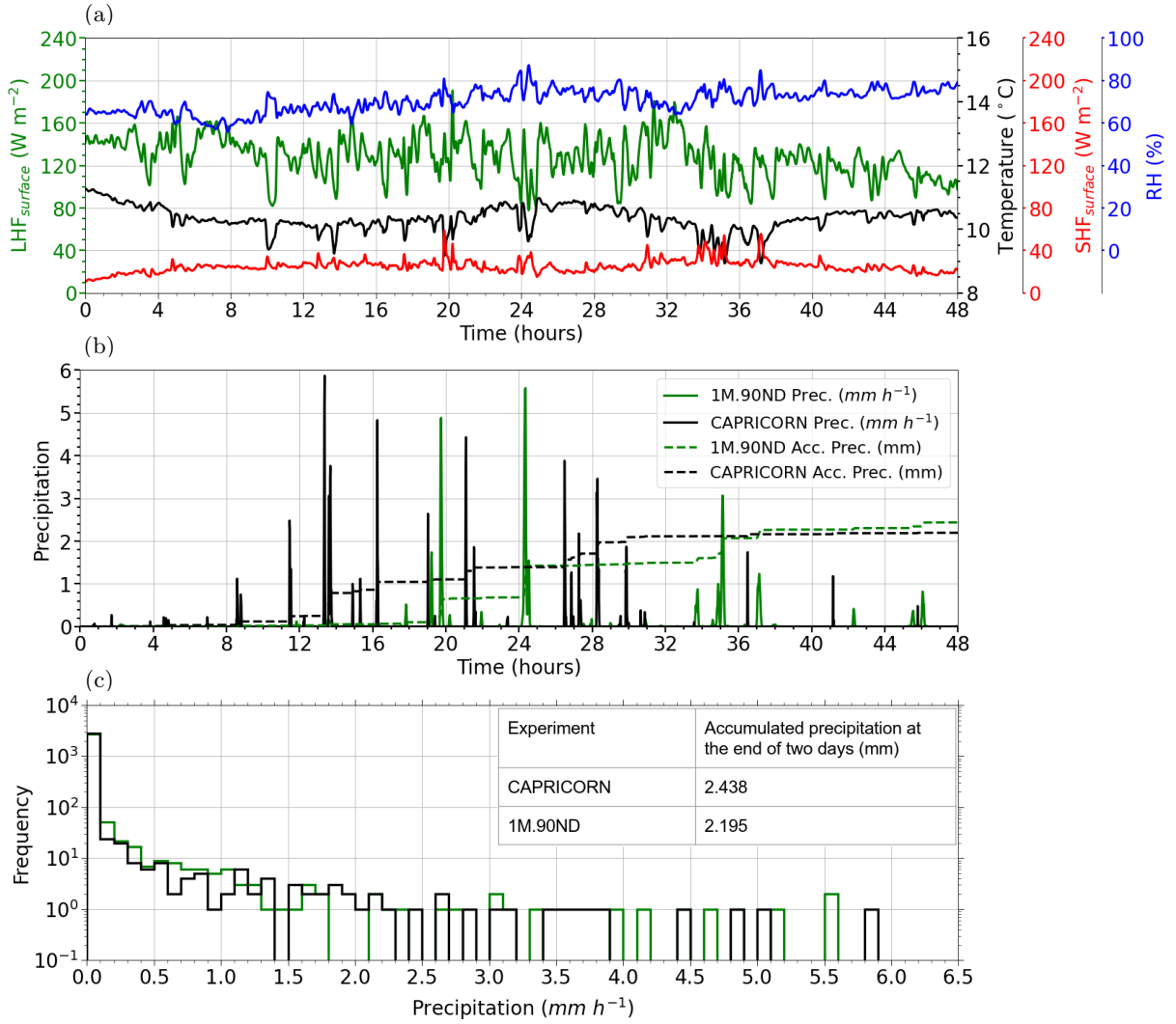


Figure 3: Time series of (a) LHF, SHF, temperature, and relative humidity for simulation, (b) simulated and observed surface precipitation rate (mm h^{-1}). (c) Histograms of precipitation rate for CAPRICORN (black) and simulation (green) along ship track. LHF, latent heat flux. SHF, sensible heat flux. The simulated data corresponds to the control simulation with a 1-min temporal resolution. Simulation period: 26th of March 2016 at 00:00:00 UTC to 28th of March 2016 at 00:00:00 UTC. Prec., precipitation rate; Acc. Prec., accumulated precipitation.

452 stable platform, which means that the observed MDV may be subject to greater uncertainty.

453 Although the reflectivity plots and CFADs provide insight into the microphysics of
 454 clouds and precipitation of the sampled SO stratocumuli, a statistical analysis of reflectivity
 455 that describes the intensity and duration of cloud-precipitation events can help us under-
 456 stand them better. Figures 4a to 4d show the fraction of cloud-precipitation events along the
 457 ship track categorized based on reflectivity between -20 and 20 dBZ incremented by a step
 458 of 10 dBZ. The fraction is calculated as the ratio of the duration of events in a reflectivity
 459 range to the total duration of cloud-precipitation events along the entire ship track. While
 460 lines and shading characterize the average intensity and duration of events, the distribution
 461 of individual dots (Figure 4e to 4h) characterizes the variability of those cloud-precipitation
 462 events. The observed lower reflectivity events (Figures 4a and 4b) dominate the cloud layer,

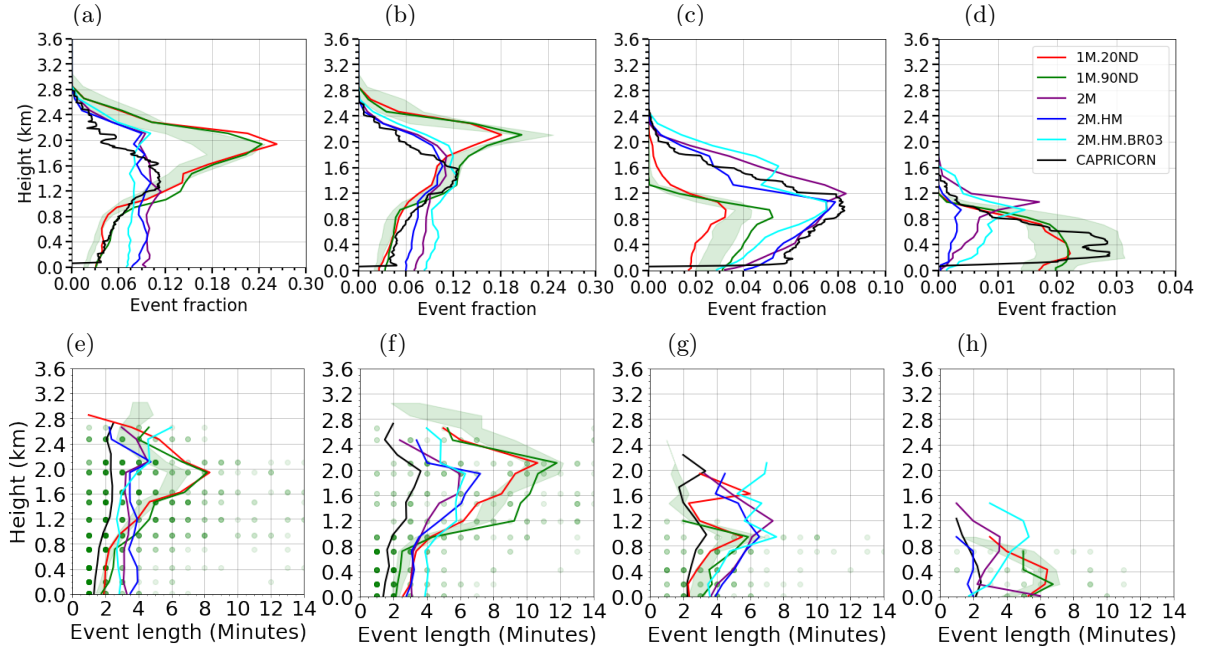


Figure 4: The cloud-precipitation occurrence (event) fraction (also termed as cloud cover) with height is categorized into reflectivity from (a) -20 to -10 dBZ, (b) -10 to 0 dBZ, (c) 0 to 10 dBZ and (d) 10 to 20 dBZ. The scatter plot represents the length of continuous cloud events with height, in the reflectivity range of (e) -20 to -10 dBZ, (f) -10 to 0 dBZ, (g) 0 to 10 dBZ and (h) 10 to 20 dBZ, where the lines represent the mean length of continuous cloud events in minutes (scatter mean). The scatter points (which are shown for control simulation only) become darker as the overlay of the data increases. The green shading corresponds to the quasi-ensemble variability (interquartile range) for the control simulation. This analysis takes into account the data throughout the ship track for the entire case period. The legends in 4d are common for all the subfigures.

463 as smaller hydrometeors (both liquid and ice) are captured in these reflectivity ranges.
 464 In a subsaturated environment, the smaller raindrops (ice crystals) evaporate (sublimate)
 465 efficiently since the surface-to-mass ratio is higher when compared with the larger raindrops
 466 (ice crystals). Since larger raindrops have higher reflectivities than solid hydrometeors
 467 (where both of them are equal in size), they are recorded in the highest reflectivity range
 468 (Figure 4d).

469 Similar distinct intermittent cloud events are simulated in 1M.90ND as were observed
 470 by the BASTA radar. However, the frequency of cloud events (Figure 4a and 4b) and their
 471 continuous duration (Figures 4e,4f) between -20 and 0 dBZ are overestimated above the
 472 melting level (approximately 1.2 km in altitude). The figures show that larger raindrops and
 473 graupel (between 0 and 10 dBZ) persist on far more successive timestamps than observed
 474 (Figure 4g), but are sparsely distributed (Figure 4c). Table S1 summarizes the range of
 475 simulated reflectivities for each hydrometeor. The simulated radar reflectivities >10 dBZ
 476 are solely due to larger raindrops. In this reflectivity range, the number of events that occur
 477 along the ship track is underestimated by 26% below 0.8 km altitude, although their mean
 478 event length is 3 times longer (Figures 4d and 4h).

479 3.2 Microphysical Sensitivities

480 We performed bulk microphysics sensitivity experiments to investigate the shortcomings
 481 of the control simulation (1M.90ND) with respect to the cloud microphysical processes, cloud
 482 occurrence, and surface precipitation. The reflectivity cross-section of the control simulation
 483 generates homogeneous clouds with constant CTHs after 36 hours of simulation time that

484 were not observed (Figures 2a and 2b). This observed variability in CTH from 36 hours
 485 onward is qualitatively better captured in all 2M simulations (Figure 2a and Figure S8). The
 486 1M simulation with reduced CDNC to 20 cm^{-3} qualitatively agrees with the arc structure of
 487 the observed CFAD (Figure 5a), however the bridge reflectivity (sum of reflectivity samples
 488 between -25 to 0 dBZ; 1.6 to 2 km altitude) reduces by 5% (Table S1c), and the bridge shifts
 489 to the left. The reduced CDNC experiment results in a decline in cloud water reflectivity
 490 and an increase in raindrop reflectivity in the CFAD bridge (Table S1). This is due to an
 491 inverse Twomey effect where the reduced CDNC leads to larger cloud droplets and more
 492 effective autoconversion. Meanwhile, it has also reduced the graupel reflectivity by 5.1%.
 493 Surprisingly, all the state-of-the-art 2M microphysics sensitivity experiments fail to achieve

dBZ	Statistics	CAP	1M.20ND	1M.90ND (ctrl)	2M.P	2M.HM	2M.HM.BR03
-40 to 20	EF	0.36	0.60	0.60	0.41	0.37	0.38
	MEL	9.10	45.41	41.33	21.25	22.0	22.92
-20 to -10	EF	0.11	0.26	0.24	0.11	0.10	0.10
	MEL	2.42	8.3	8.15	3.25	3.49	3.93
-10 to 0	EF	0.13	0.18	0.21	0.11	0.11	0.12
	MEL	2.77	9.30	10.67	5.98	7.21	6.32
0 to 10	EF	0.08	0.03	0.05	0.08	0.08	0.07
	MEL	2.0	3.0	2.0	3.29	4.5	6.88
10 to 20	EF	0.03	0.02	0.02	0.02	<0.01	0.01
	MEL	1.0	3.0	5.0	1.0	1.0	3.0

Table 2: Reflectivity statistics derived from Figure 4. ‘EF’ is the event fraction of the simulations and CAPRICORN at the altitude where their maximum event fraction occurs. ‘MEL’ is the mean event length (min) of the simulations and CAPRICORN at the altitude where the maximum event fraction of the respective simulation and CAPRICORN occurs. CAP, CAPRICORN. ctrl, control simulation.

494 the CFAD reflectivity arc, which is a proxy for cloud-precipitation vertical structure. The
 495 mean contribution of the graupel bridge reflectivity is reduced by 80% for 2M microphysics
 496 experiments and the mean increase in graupel for the experiments with secondary ice pro-
 497 cesses is just 23% with respect to 2M.P. Irrespective of the increase in rain and snow re-
 498 flectivities in all 2M simulations, the reflectivity of the bridge is reduced by 46% (49%)
 499 with respect to the control simulation (BASTA radar). This demonstrates the importance
 500 of graupel processes in the SO mixed-phase Sc clouds sampled during CAPRICORN. The
 501 variations in hydrometeors other than graupel in the bridge are also noticeable, although
 502 the largest value of total graupel reflectivity due to its size and number concentration makes
 503 it dominant in the cloud layer (Table S1b). Meanwhile, the 2M.HM simulation generates
 504 very small cloud particles as their maximum reflectivity is 2.6 times less than the control
 505 simulation (Figure 2f and 5c).

506 In Table 2, the mean event (cloud-precipitation) length and the occurrence fraction have
 507 been derived for all experiments at the altitude of their maximum mean event fraction. All
 508 simulated values are overestimated. However, the 2M experiments show a better agreement
 509 with the observations than the 1M simulations. For all simulations, this agreement does not
 510 hold true across all altitudes. This shows that the microphysics of ICON simulations (1M
 511 and 2M) do not perfectly replicate the observed cloud vertical structure along the ship track.
 512 Figure 6 shows the simulated and observed surface precipitation along the ship track for the
 513 entire case period. All simulations except 2M.HM.BR03 show intense precipitation, hence
 514 the change in the accumulated precipitation in 2M.HM.BR03 is gradual at all timestamps.
 515 As expected, none of the experiments replicate the timing of the precipitation rate, the pro-
 516 file and variability of accumulated precipitation as compared to the observation. Although
 517 all the single track simulated data (except 2M.HM.BR03) overestimate the accumulated

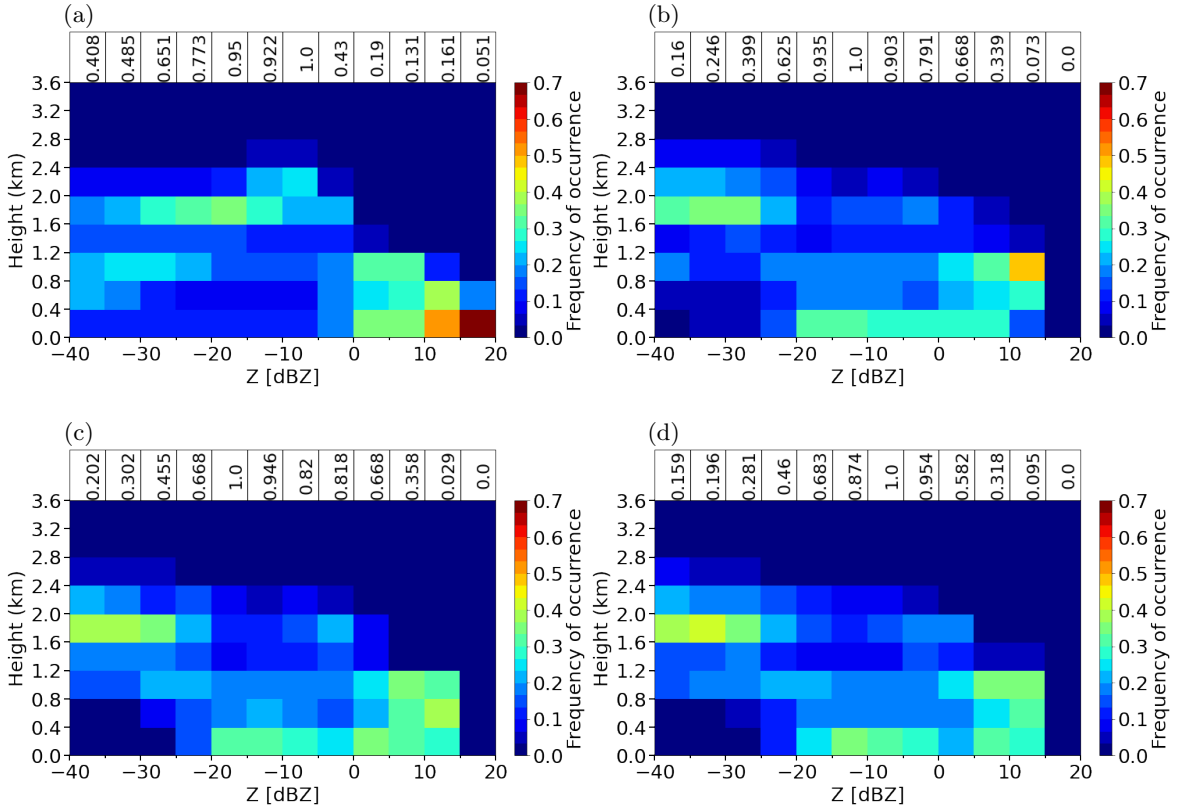


Figure 5: Contoured frequency by altitude diagrams (CFAD) with 1-min temporal resolution for the entire case study period of a) 1M.20ND, (b) 2M.P (c) 2M.HM and (d) 2M.HM.BR03. CFAD is normalized with the total samples in every reflectivity bin. The numerical data at the top of CFAD are the ratios of cumulated samples in every reflectivity bin to the highest cumulated samples from all the reflectivity bins. Case study period: 26th of March 2016 at 00:00:00 UTC to 28th of March 2016 at 00:00:00 UTC.

518 precipitation along the ship track at the end of two days, the ensemble accumulated precipi-
 519 tation variability (interquartile range) for 1M.90ND (the full variability is available only for
 520 1M.90ND due to output limitation) increases with time, and further overlaps with that of
 521 other experiments (in particular during a large time period on 27th of March 2016). While
 522 the observations are entirely within the spatio-temporal variability of 1M.90ND, a maximum
 523 of 66% for 2M.P and a minimum of 21% for 2M.HM.BR03 overlap with the variability of
 524 1M.90ND. This suggests that due to the small sample size (two-day) and wide confidence
 525 interval (provided the ensemble variability within each experiment is significant), it remains
 526 difficult to characterize the full spatio-temporal variability of the surface precipitation.

527 The simulated domain mean surface precipitation (domain mean CB precipitation
 528 rates) are 0.045 mm hr⁻¹ (3.6 mm hr⁻¹) for 2M.P, 0.053 mm hr⁻¹ (3.3 mm hr⁻¹) for 2M.HM,
 529 and 0.061 mm hr⁻¹ (2.7 mm hr⁻¹) for 2M.HM.BR03. This shows that despite a mean in-
 530 crease in total ice number concentration by two (three) orders of magnitude for 2M.HM
 531 (2M.HM.BR03) compared with 2M.P (Figure S9), the mean surface precipitation rate only
 532 modestly increases, and the CB precipitation rate even decreases. This result is somewhat
 533 counter-intuitive as one would expect increased cloud glaciation due to increased ICNC and
 534 thus increased growth rates by deposition (e.g. Vergara-Temprado et al. (2018)). Yet, CB
 535 precipitation rates decrease in our simulations. We cannot uniquely identify what is causing
 536 this decrease by 6% in 2M.HM and 23% in 2M.HM.BR03 with respect to 2M.P. However,
 537 the following processes may play a role. Firstly, the rate of ice hydrometeor growth through
 538 riming with cloud droplets is decreased in 2M.HM.BR03 which further reduces CB precipi-

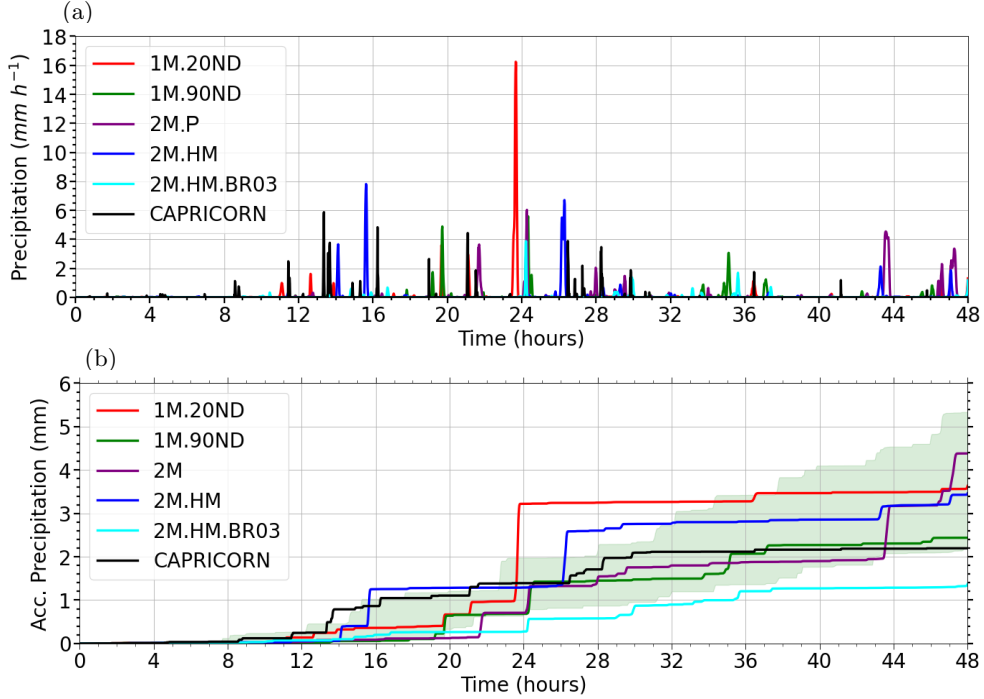


Figure 6: Time series of simulated and observed (a) precipitation rate (mm h^{-1}) and (b) accumulated precipitation (mm). Simulated data corresponds to control simulation and all the simulations in the bulk microphysical sensitivity analysis. The green shading corresponds to the quasi-ensemble variability (25th and 75th percentiles) of accumulated precipitation for the control simulation.

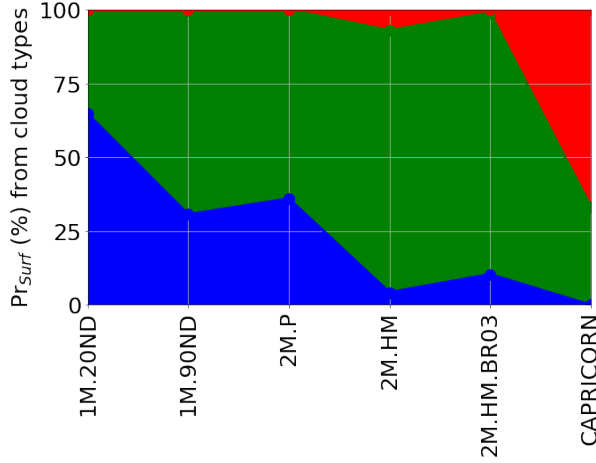


Figure 7: The relative percentage contribution of various cloud types (liquid - blue, mixed - green and ice - red) to surface precipitation along the ship track is stacked on top of one another. Data is analyzed for the entire case study period (26th of March 2016 at 00:00:00 UTC to 28th of March 2016 at 00:00:00 UTC).

539 tation (Figure S10). Secondly, the very small ejected ice crystals during collisional breakup
 540 may not be favorable for the formation of snow (ice-ice aggregation) and growth of snow
 541 (ice-snow collision). Thirdly, unlike HM, collisional breakup reduces the size and eventually
 542 the mass of individual solid hydrometeors by ice fragmentation, thus reducing their termi-
 543 nal fall velocity. Fourthly, while depositional growth increases, it does not compensate for

544 the decrease in size by fragmentation. Thus terminal fall velocity remains low. It is likely
 545 that combined effect of: reduced terminal fall speed of ice crystals, and decreased riming
 546 efficiencies, reduce the mean CB precipitation rate in 2M.HM.BR03 as compared to 2M.HM.

547 Figure 7 shows the simulated cloud type contribution to surface precipitation rates.
 548 Here, the cloud types are categorized as liquid (liquid CB with liquid CB precipitation), ice
 549 (ice CB with ice CB precipitation), and mixed (CB and CB precipitation having different
 550 phases). The Twomey effect is illustrated clearly by the drop of 29% in liquid cloud con-
 551 tribution to precipitation rates between 1M.20ND and 1M.90ND. The ice (mixed) clouds
 552 contribute 67% (33%) to the observed precipitation rates, and the impact of ice (mixed)
 553 clouds on all the simulations is lower (higher). Ice and mixed-phase clouds account for
 554 an increase of 32% in surface precipitation rates from 2M.P to 2M.HM, but this fraction
 555 decreases by 6% from 2M.HM to 2M.HM.BR03. The fractional decline could be explained
 556 by the fact that (i) smaller ice particles require less latent heat to melt, as they cross the
 557 melting line within the cloud layer and (ii) reduced ice mass sedimentation as stated in the
 558 previous paragraph.

559 3.3 Impacts on Radiation

560 Figure 8a shows the observed and simulated surface downwelling SW radiation ($SW_{\text{surf,down}}$),
 561 as well as the liquid, mixed, and ice CT fractions. In general, we find that the lower the com-
 562 bined liquid and mixed CT fraction, the higher the mean $SW_{\text{surf,down}}$ is in all the simulations.
 563 This is entirely consistent with the larger scattering efficiency of the far more numerous and
 564 smaller cloud droplets as compared the few and large ice crystals (Greenwald et al., 1995).
 565 We further observe that changes in cloud phase area fraction have a considerably larger
 566 impact on $SW_{\text{surf,down}}$ than microphysical effects such as Twomey. An increase in ice-phase
 567 fraction in 2M.HM.BR03 with respect to 2M.HM increases $SW_{\text{surf,down}}$ by 8 W m^{-2} . This
 568 is twice as large as the decrease through the Twomey effect by 4 W m^{-2} between 1M.20ND
 569 and 1M.90ND. Hence, these two simulations (2M.HM and 2M.HM.BR03) generate optically
 570 thicker clouds. In all other simulations the underestimation in $SW_{\text{surf,down}}$ is likely caused
 571 by both: an overabundance of liquid-containing clouds and overestimated optical depth.

572 As discussed above, CTP plays a predominant role in constraining the cloud-top radiative
 573 effect. The histograms of relative occurrences of CTP binned into 5°C CTT are shown
 574 in Figure 8b. The sampled open-cell (36 hours from 26th of March 2016 at 06:00:00 UTC)
 575 CTP from HIMAWARI along the ship track is classified with 78.3% as liquid. The total liq-
 576 uid fraction consists of 49.8% warm liquid water (LW) and 28.5% SLW. Meanwhile, merely
 577 5.9% of all clouds in the control simulation are classified as liquid at CT with 1.1% LW and
 578 4.8% SLW. The narrowly distributed simulated CTT with the mode between -10°C and
 579 -5°C holds 75.6% mixed-phase CTs against the observed 3.1%. Further, HIMAWARI clas-
 580 sifies only 8.5% as mixed-phase open-cell stratocumuli at CT along the ship track, whereas
 581 87.78% are identified as such in the control simulation. This may be due to the lower verti-
 582 cal resolution, inadequate representation of CT turbulence, dissipation of the sharp tempera-
 583 ture inversion due to TKE centered around the CT instead of being at or below the CT,
 584 poor updraft velocity to push cloud droplets to the CT (Vignon et al., 2021), and possibly
 585 overprediction of ICNC by the temperature-dependent Cooper parameterization for ice nu-
 586 cleation (Cooper, 1986). No open-cell Sc CTTs are simulated (1M.90ND) below -15°C and
 587 above 5°C , whereas 13.1% (ice) and 21.8% (LW) CTs were observed below and above these
 588 limits along the ship track. However, the warm clouds in HIMAWARI may be subject to
 589 large uncertainties since the surface temperature and emissivity influence the CTT retrievals
 590 (Huang et al., 2019). Overall, the control simulation along the ship track (open-cell period)
 591 overestimates the liquid and mixed-phase CTs by 35.2%, and overestimates the cloud oc-
 592 currence by 26.1%, resulting in the underestimation of surface downwelling SW radiation
 593 by 42.7%, compared to the observations.

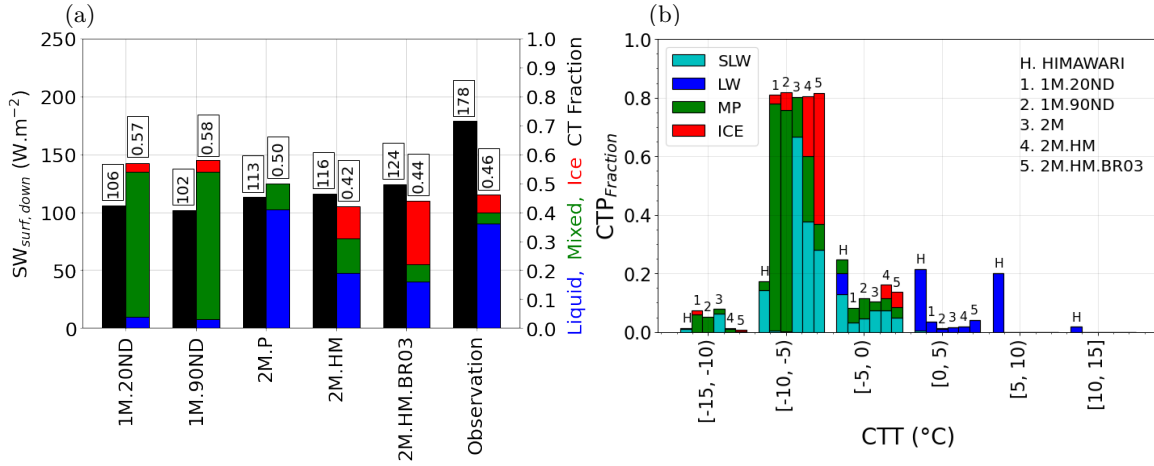


Figure 8: HIMAWARE and simulated data along the ship track during the open-cell period. (a) Surface downwelling shortwave radiation ($W \cdot m^{-2}$) and the total CT fractions with relative contributions of liquid (blue), mixed (green), and ice (red) phase (stacked one over the other). (b) Histograms of CTP fractions as a function of the cloud-top temperature (CTT) with the bins of $5^{\circ}C$. CT, cloud-top. HIMAWARE data is obtained from Huang et al. (2019); Lang et al. (2021).

594 Although the CTP distinguished with CTT doesn't vary substantially for the reduced
 595 CCN experiment (1M.20ND), the occurrence of SLW significantly increases in the 2M ex-
 596 periments between $-10^{\circ}C$ and $-5^{\circ}C$ (Figure 8b). Since many cloud event streaks are entirely
 597 liquid with no traces of solid hydrometeors (Figure S11), they increase the CT SLW frac-
 598 tion. As opposed to the Cooper ICNC curve, the observationally constrained INP immersion
 599 freezing parameterization with considerably lower INP background concentrations has pro-
 600 duced MPCs only at a few instances along the ship track. Although, the in-cloud domain
 601 mean IWP has increased to $50 g \cdot m^{-2}$ in the 2M.P simulation (Figure S9). This shows that
 602 the immersion INP parameterization adjusted for the SO remote region is insufficient to
 603 reduce cloud-radiative biases caused by inaccurate representations of cloud phase and the
 604 partitioning of the total water path between LWP and IWP. Similar to the control simula-
 605 tion, all the sensitivity experiments cluster 80% of the simulated CTs between $-10^{\circ}C$ and
 606 $-5^{\circ}C$. Warm CTs above $5^{\circ}C$ are still missing. However, the increase in the ice occurrence
 607 fraction at CT is consistent with the activation of secondary ice processes between $-10^{\circ}C$
 608 and $-5^{\circ}C$ (2M.HM and 2M.HM.BR03).

3.4 Perturbed-Parameter Experiments to enhance graupel formation in 2M simulations

611 As discussed in section 3.2, the state-of-the-art 2M microphysics scheme in ICON dis-
 612 plays stronger biases in the vertical structure of precipitation than the 1M simulations. Here,
 613 we look at the microphysical pathways to understand the role of individual processes for
 614 both schemes in detail (Figure 9). As discussed earlier, graupel particles play a significant
 615 role in the occurrence of the bridge in the cloud layer in CFAD diagrams. The time-height
 616 cross-section of the simulated phase shows that graupel (hatching in figures) covers a larger
 617 sample in 1M (Figure 2d and Figure S11a) than in all the 2M simulations (Figures S11b to
 618 S11d) above the melting level. The 1M and 2M microphysical pathway analysis discussed in
 619 this section is obtained from the 1M.90ND and 2M.HM simulations on 27th of March 2016.
 620 Among the graupel growth processes shown in Figure S12 and Figure 9, CG2G_rim (cloud-
 621 graupel to graupel riming) and RG2G_rim (rain-graupel to graupel riming) are the dominant
 622 processes. The CG2G_rim process rate is higher in the cloud layer in the 1M scheme (9.13)
 623 than in the 2M scheme (2.30). Note that all process rates are normalized for comparability
 624 by WVl as described in section 2.3 and are thus unitless. Although RG2G_rim is not

Expt No.	Description	CG2G _rim	G2R _melt	RG2G _rim	G _dep	G _budget
1	2M.HM * E10	24.80	-108.06	77.52	5.41	9.00
2	2M.P	-14.37	-16.46	-12.09	-31.41	-19.47
3	2M.HM.BR03	5.12	6.75	5.28	1.35	6.08
4	CCN10	-1.09	-8.57	-9.60	-11.59	-7.54
5	CCN1000	-39.71	-45.93	-49.67	-34.84	-41.79
6	aukcc*0.5	2.32	3.88	4.37	0.88	0.72
7	aukcc*2	-1.23	-5.95	-6.91	-1.24	-0.55
8	ice_vel_coef	3.85	-4.04	-5.63	-2.83	-0.32
9	rain_atlas	-6.90	-4.87	-3.59	-3.96	-6.25
10	agg_50	1.45	0.94	1.10	0.53	0.99
11	agg_200	-4.41	-2.17	-2.97	-3.64	-2.61
12	gr_d_m	-7.90	-8.53	-9.65	-7.08	0.96
13	gr_d_h	-16.56	-21.51	-24.15	-2.76	5.61
14	gr_v_h	-3.29	-9.28	-12.13	-38.94	-51.70
15	gr_max_dia	-63.85	-76.84	-81.73	-59.72	-60.49

Table 3: The top row (in kg) shows the sum of the product of hourly process rates and volume of each cell for the reference simulation (2M.HM) on 27th of March 2016. G_budget (in kg) for the reference simulation refers to the sum of the product of instantaneous graupel mass density and the volume of each cell. All the other rows are percentage changes with respect to the reference simulation. The intensity of the color scale shows the percentage decrease (increase) in red (blue). The table only shows process budgets that exceeded 50% of the G_budget.

652 To realistically simulate the graupel processes in the SO Sc clouds, it is crucial to
653 analyze their sensitivity to the parameters related to CCN and ice-phase processes. Our
654 small parameter ensemble is motivated by the importance of CG2G_rim and RG2G_rim for
655 graupel growth. CCN concentrations are perturbed for the former, and the rain terminal
656 velocity relation (power-law (Seifert & Beheng, 2006), and atlas-law (Seifert et al., 2014)),
657 as a function of its mass, is perturbed for the latter. As reported in Seifert and Beheng
658 (2006), the velocity coefficients of ice crystals are based on the measurements from Locatelli
659 and Hobbs (1974); Heymsfield and Kajikawa (1987). Furthermore, the graupel density and
660 its velocity measured during the winter months of 1971-1972 and 1972-1973 in the Cascade
661 Mountains of Washington (Locatelli & Hobbs, 1974) are used to study the sensitivity of the
662 G_budget.

663 The 2M.HM simulation (Table 3) is considered a reference experiment in this section.
664 The numbers, except for the G_budget in the reference experiment, are averaged hourly and
665 summed over a time period of 24 hours on 27th of March, 2016. The G_budget in the last
666 column of this experiment refers to the time-space integrated sum of instantaneous hourly
667 graupel mass mixing ratios for the same 24 hours period. All the other rows in this table
668 represent the percentage change with respect to the reference simulation. The increase in
669 CCN from 10 cm^{-3} to 1000 cm^{-3} results in a monotonic increase in smaller cloud droplets
670 (Twomey & Warner, 1967). This reduces the cloud droplet autoconversion and accretion
671 rates, and further delays the rain to graupel riming process. The net G_budget is reduced
672 by 41.79%. Similarly, reducing the CCN (CCN10) below a threshold value also reduces the
673 G_budget and the related process rates. A reduced autoconversion kernel coefficient by a
674 factor of 2 increased the rate of the cloud-graupel riming process by 2.3%, since the rain
675 particle formation slowed down. This modest increase could be attributed to the lower cloud
676 liquid water path (LWP) in 2M simulations compared to 1M simulations. Any increase in
677 graupel density allows for an increase in its mass and hence a modest gain in the G_budget.
678 However, the mass and terminal velocity of the hydrometeors are coupled by a power-law.
679 An increase in graupel density or graupel diameter increases the terminal velocity which

680 reduces its residence time, and hence the G_budget (experiments 13 and 14 in Table 1).
 681 The rime splintering process reduces the gap between the simulated and observed ICNC,
 682 and also governs the new graupel particle formation processes (experiment no. 15 in Table
 683 1) in the remote environment of the SO boundary layer. Hence, the secondary ice production
 684 processes (HM and collisional breakup) lead to an increase in the net G_budget.

685 Overall, it is significant that (i) the CCN number concentration affects the G_budget
 686 through the RG2G_riming process and (ii) the graupel properties (density, velocity, and size)
 687 have a strong effect on the net G_budget. The 2M microphysics sensitivity experiments for
 688 SO Sc clouds show that the net G_budget is at its maximum when: (i) the graupel density,
 689 velocity, and size are low, (ii) the power-law captures the raindrop velocity as a function of
 690 its mass, (iii) secondary ice production processes are active, and (iv) CCN values are low.

691 4 Discussion and Conclusions

692 We have evaluated the ability of kilometer-scale ICON real-case simulations against
 693 the observed cloud and precipitation statistics derived from remote sensing and in-situ mea-
 694 surements during CAPRICORN. In general, the control simulation captured the observed
 695 cloud-precipitation vertical structure due to graupel growth by the riming of cloud droplets.
 696 A continuous formation of graupel, its growth in the cloud layer, and subsequent melting
 697 are crucial processes for realistically representing the cloud-precipitation vertical structure
 698 of SO Sc clouds. Further, a lower CCN concentration and increased density, velocity, and
 699 size of graupel particles all enhance low-cloud graupel formation. According to the micro-
 700 physical pathway analysis, graupel melting is a major source of SO Sc precipitation during
 701 CAPRICORN. The duration of continuous cloudy elements containing either cloud droplets,
 702 rain, or graupel particles is overestimated in all ICON simulations. This results in an over-
 703 estimated mean duration of cloudy elements along the entire ship track. Thus, the timing
 704 of the simulated cloud-precipitation events doesn't agree with CAPRICORN, which is also
 705 evident in the comparison with observed surface precipitation rates. The simulated surface
 706 precipitation is sparsely dispersed, whereas the OceanRAIN disdrometer measures densely
 707 distributed precipitation rates with relatively sharp spikes. Although the simulated accu-
 708 mulated precipitation at the end of two days is closer to CAPRICORN, the onset of stronger
 709 precipitation in the open-cell region is delayed by 9 hours in the simulation. Although the
 710 observations are within the simulated range of variability of the control simulation, longer
 711 continuous observations within the same cloud regime would be needed to fully constrain the
 712 simulated cloud-precipitation statistics. Despite these shortcomings, the control simulation
 713 captured the surface cold pool (drop in near-surface air temperature) in many timestamps
 714 that favored the occurrence of the transition layer and the decoupling of the boundary layer.

715 The phase distinction from the merged radar-lidar product, the CFAD of radar reflectivity,
 716 and the HIMAWARI CTP confirm the presence of ice in the cloud. We observed
 717 that the bridge reflectivity (reflectivity of a sharp horizontal band in the arc i.e., in the
 718 cloud layer) is a reasonable proxy for evaluating the cloud layer hydrometeors. According to
 719 the independent hydrometeor reflectivity contribution analysis for all simulations, a relative
 720 increase in the graupel mass in the cloud layer reduced the gap between the observed and
 721 simulated bridge reflectivities, resulting in a more realistic representation of the arc struc-
 722 ture. The highest contribution of graupel is 66% (1M.90ND) and 59% (1M.20ND) in 1M
 723 simulations that realistically represent the observed cloud vertical structure, while it is less
 724 than 20% in 2M simulations. In addition to the occurrence of graupel in the cloud layer, all
 725 other processes involving graupel and raindrops, such as partially sublimated frozen parti-
 726 cles, partially evaporated larger raindrops, melting of graupel, raindrop selfcollection, and
 727 solid hydrometeors coated with liquid layer during the collision of ice particles with rain-
 728 drops are also crucial in describing the observed cloud-precipitation vertical structure. The
 729 raindrops in the cloud layer (bridge) dominate the reflectivities rather than the graupel in
 730 all 2M simulations. The enhanced raindrop reflectivity in the cloud layer did not increase
 731 bridge reflectivity, rather, the bridge reflectivity decreased by 46% compared to the control

732 simulation. Theoretically, graupel (rain) contributed reflectivities could be increased (de-
 733 creased) if efficient in-cloud graupel growth by riming rain scavenges raindrops. Hence, the
 734 bridge statistics clearly emphasize the significance of graupel in SO Sc clouds.

735 The presence of graupel, which is one of the necessary conditions in HM (Hallett &
 736 Mossop, 1974) and an enhancing parameter due to increased collisional kinetic energy in
 737 breakup collisions (Phillips, Yano, & Khain, 2017), increases the secondary ice production.
 738 We investigated the sensitivity with respect to secondary ice generating processes (HM and
 739 collisional breakup) in Sc clouds during CAPRICORN. The maximum reflectivity of cloud
 740 droplets in the 2M.HM simulation is 2.6 times lower than the control simulation, indicating
 741 that cloud droplet size decreased. The reflectivity event fractions of all the 2M simulations
 742 show that the larger raindrops ($20 > \text{dBZ} > 10$) evaporate effectively in the sub-cloud layer
 743 and increase the smaller raindrop number concentration in the intermediate reflectivity
 744 range ($10 > \text{dBZ} > -20$), and hence the occurrence of strong frequency of occurrence band
 745 near the surface in the 2M CFAD diagrams. This indicates that the near-surface raindrops
 746 in all 2M simulations are smaller compared to 1M simulations. Although the domain mean
 747 total ice number concentration (total ice water path) in 2M.HM.BR03 increase by roughly
 748 10 (1.4) times compared to 2M.HM, the domain mean precipitation increases by just 1.2
 749 times. Hence, despite the increase in the total ice number concentration through collisional
 750 breakup, the precipitation statistics remain dominated by melted graupel containing primary
 751 INP along the ship track.

752 The $\text{SW}_{\text{surf,down}}$ along the ship track in the control simulation is negatively biased
 753 by 43% due to the overestimation of the liquid and mixed-phase CT by 35%, and the
 754 cloud occurrence by 26%. Furthermore, the $\text{SW}_{\text{surf,down}}$ of all simulations is negatively
 755 biased irrespective of the extent of liquid CT fraction, yet, most of the simulated total
 756 liquid and mixed-phase CT fractions are higher than observed during CAPRICORN. The
 757 control simulation failed to produce the dominant liquid CTs, instead, 87.78% are mixed-
 758 phase with just 8.5% diagnosed as such in HIMAWARI retrievals. This could be due to a
 759 variety of factors, one of which is the insufficient vertical resolution in all simulations that
 760 would be required to fully represent a supercooled liquid layer on top of the mixed-phase
 761 cloud. It is worth noting that the 2M simulations (2M.HM and 2M.HM.BR03) adjusted
 762 for a remote INP environment over the SO generate optically thicker clouds, as primary
 763 nucleation is considerably reduced and indeed many cloud profiles are entirely liquid. All
 764 other simulations generate positively biased cloud cover and/or optically thicker clouds.
 765 Thus the cloud radiative bias in this particular regime is contrary to the climatological bias
 766 (Trenberth & Fasullo, 2010; Bodas-Salcedo et al., 2014; Vergara-Temprado et al., 2018).

References

- 767
- 768 Ahn, E., Huang, Y., Chubb, T. H., Baumgardner, D., Isaac, P., de Hoog, M., . . . Manton,
769 M. J. (2017). In situ observations of wintertime low-altitude clouds over the Southern
770 Ocean. *Quarterly Journal of the Royal Meteorological Society*, *143*(704), 1381–1394.
771 doi: 10.1002/qj.3011
- 772 Alexander, S. P., & Protat, A. (2018). Cloud Properties Observed From the Surface and
773 by Satellite at the Northern Edge of the Southern Ocean. *Journal of Geophysical
774 Research: Atmospheres*, *123*(1), 443–456. doi: 10.1002/2017JD026552
- 775 Bechtold, P., Köhler, M., Jung, T., Doblas-Reyes, F., Leutbecher, M., Rodwell, M. J.,
776 . . . Balsamo, G. (2008, jul). Advances in simulating atmospheric variability with
777 the ECMWF model: From synoptic to decadal time-scales. *Quarterly Journal of
778 the Royal Meteorological Society*, *134*(634), 1337–1351. Retrieved from [https://
779 onlinelibrary.wiley.com/doi/10.1002/qj.289](https://onlinelibrary.wiley.com/doi/10.1002/qj.289) doi: 10.1002/qj.289
- 780 Bodas-Salcedo, A., Williams, K. D., Field, P. R., & Lock, A. P. (2012). The surface
781 downwelling solar radiation surplus over the southern ocean in the met office model:
782 The role of midlatitude cyclone clouds. *Journal of Climate*, *25*(21), 7467–7486. doi:
783 10.1175/JCLI-D-11-00702.1
- 784 Bodas-Salcedo, A., Williams, K. D., Ringer, M. A., Beau, I., Cole, J. N., Dufresne, J. L., . . .
785 Yokohata, T. (2014). Origins of the solar radiation biases over the Southern Ocean in
786 CFMIP2 models. *Journal of Climate*, *27*(1), 41–56. doi: 10.1175/JCLI-D-13-00169.1
- 787 Bosello, F., Roson, R., & Tol, R. S. J. (2007, may). Economy-wide Estimates
788 of the Implications of Climate Change: Sea Level Rise. *Environmental and Resource Economics*,
789 *37*(3), 549–571. Retrieved from [http://
790 dx.doi.org/10.1038/s41561-018-0234-1](http://dx.doi.org/10.1038/s41561-018-0234-1)[http://www.atmos.washington.edu/
791 {~}sgw/PAPERS/2007/{~}ndp026e.pdf](http://www.atmos.washington.edu/~sgw/PAPERS/2007/{~}ndp026e.pdf)[https://journals.ametsoc.org/doi/pdf/
792 10.1175/1520-0477\(1984\)065{~}3C1290:OFROSM{~}3E2.0.CO{~}3B2](https://journals.ametsoc.org/doi/pdf/10.1175/1520-0477(1984)065{~}3C1290:OFROSM{~}3E2.0.CO{~}3B2)[http://
793 link.springer.com/10.1007/s10640-006-9048-5](http://link.springer.com/10.1007/s10640-006-9048-5) doi: 10.1007/s10640-006-9048-5
- 794 Bretherton, C. S., & Wyant, M. C. (1997). Moisture transport, lower-tropospheric stability,
795 and decoupling of cloud-topped boundary layers. *Journal of the Atmospheric Sciences*,
796 *54*(1), 148–167. doi: 10.1175/1520-0469(1997)054<0148:MTL TSA>2.0.CO;2
- 797 Caughey, S. J., Crease, B. A., & Roach, W. T. (1982). A field study of nocturnal strato-
798 cumulus II Turbulence structure and entrainment. *Quarterly Journal of the Royal
799 Meteorological Society*, *108*(455), 125–144. doi: 10.1002/qj.49710845508
- 800 Cooper, W. A. (1986, dec). Ice Initiation in Natural Clouds. *Meteorological Monographs*,
801 *43*(43), 29–32. Retrieved from [https://journals.ametsoc.org/view/journals/
802 amsm/21/43/0065-9401-21{~}43{~}29.xml](https://journals.ametsoc.org/view/journals/amsm/21/43/0065-9401-21{~}43{~}29.xml)[http://journals.ametsoc.org/doi/
803 10.1175/0065-9401-21.43.29](http://journals.ametsoc.org/doi/10.1175/0065-9401-21.43.29) doi: 10.1175/0065-9401-21.43.29
- 804 Delanoë, J., Protat, A., Vinson, J. P., Brett, W., Caudoux, C., Bertrand, F., . . . Dupont,
805 J. C. (2016). BASTA: A 95-GHz FMCW Doppler radar for cloud and fog studies.
806 *Journal of Atmospheric and Oceanic Technology*, *33*(5), 1023–1038. doi: 10.1175/
807 JTECH-D-15-0104.1
- 808 Demott, P. J., Prenni, A. J., McMeeking, G. R., Sullivan, R. C., Petters, M. D., Tobo,
809 Y., . . . Kreidenweis, S. M. (2015). Integrating laboratory and field data to quantify
810 the immersion freezing ice nucleation activity of mineral dust particles. *Atmospheric
811 Chemistry and Physics*, *15*(1), 393–409. doi: 10.5194/acp-15-393-2015
- 812 Doms, G., Förstner, J., Heise, E., Herzog, H.-J., Mironov, D., Raschendorfer, M., . . .
813 Vogel, G. (2011). A description of the Nonhydrostatic Regional COSMO Model,
814 Part II: Physical parameterization. Deutscher Wetterdienst: Offenbach, Germany.
815 *Www.Cosmo-Model.Org*(September), 152. doi: <http://www.cosmo-model.org>
- 816 Fiddes, S. L., Protat, A., Mallet, M. D., Alexander, S. P., & Woodhouse, T. (2022). Southern
817 Ocean cloud and shortwave radiation biases in a nudged climate model simulation :
818 does the model ever get it right ? *Atmospheric Chemistry and Physics Discussions*,
819 *Preprint*(April), 1–34. Retrieved from [https://acp.copernicus.org/preprints/
820 acp-2022-259/acp-2022-259.pdf](https://acp.copernicus.org/preprints/acp-2022-259/acp-2022-259.pdf)
- 821 Fridlind, A. M., Ackerman, A. S., McFarquhar, G., Zhang, G., Poellot, M. R., DeMott,

- 822 P. J., ... Heymsfield, A. J. (2007). Ice properties of single-layer stratocumulus during
 823 the Mixed-Phase Arctic Cloud Experiment: 2. Model results. *Journal of Geophysical*
 824 *Research Atmospheres*, *112*(24), 1–25. doi: 10.1029/2007JD008646
- 825 Greenwald, T. J., Stephens, G. L., Christopher, S. A., & Vonder Haar, T. H.
 826 (1995, dec). Observations of the Global Characteristics and Regional Ra-
 827 diative Effects of Marine Cloud Liquid Water. *Journal of Climate*, *8*(12),
 828 2928–2946. Retrieved from [http://journals.ametsoc.org/doi/10.1175/1520-](http://journals.ametsoc.org/doi/10.1175/1520-0442(1995)008<2928:OOTGCA>2.0.CO;2)
 829 [0442\(1995\)008{\\%}3C2928:OOTGCA{\\%}3E2.0.CO;2](http://journals.ametsoc.org/doi/10.1175/1520-0442(1995)008<2928:OOTGCA>2.0.CO;2) doi: 10.1175/1520-0442(1995)
 830 008<2928:OOTGCA>2.0.CO;2
- 831 Hallett, J., & Mossop, S. C. (1974, may). Production of secondary ice particles during the
 832 riming process. *Nature*, *249*(5452), 26–28. Retrieved from [https://www.nature.com/](https://www.nature.com/articles/249026a0)
 833 [articles/249026a0](https://www.nature.com/articles/249026a0) doi: 10.1038/249026a0
- 834 Heymsfield, A. J., & Kajikawa, M. (1987, apr). An Improved Approach to Calculating
 835 Terminal Velocities of Plate-like Crystals and Graupel. *Journal of the Atmospheric*
 836 *Sciences*, *44*(7), 1088–1099. Retrieved from [http://journals.ametsoc.org/doi/](http://journals.ametsoc.org/doi/10.1175/1520-0469(1987)044<1088:AIATCT>2.0.CO;2)
 837 [10.1175/1520-0469\(1987\)044{\\%}3C1088:AIATCT{\\%}3E2.0.CO;2](http://journals.ametsoc.org/doi/10.1175/1520-0469(1987)044<1088:AIATCT>2.0.CO;2) doi: 10.1175/
 838 1520-0469(1987)044<1088:AIATCT>2.0.CO;2
- 839 Hu, Y., Rodier, S., Xu, K. M., Sun, W., Huang, J., Lin, B., ... Josset, D. (2010). Occur-
 840 rence, liquid water content, and fraction of supercooled water clouds from combined
 841 CALIOP/IIR/MODIS measurements. *Journal of Geophysical Research Atmospheres*,
 842 *115*(19), 1–13. doi: 10.1029/2009JD012384
- 843 Hu, Y., Winker, D., Vaughan, M., Lin, B., Omar, A., Trepte, C., ... Kuehn, R. (2009).
 844 CALIPSO/CALIOP cloud phase discrimination algorithm. *Journal of Atmospheric*
 845 *and Oceanic Technology*, *26*(11), 2293–2309. doi: 10.1175/2009JTECHA1280.1
- 846 Huang, Chubb, T., Baumgardner, D., DeHoog, M., Siems, S. T., & Manton, M. J. (2017).
 847 Evidence for secondary ice production in Southern Ocean open cellular convection.
 848 *Quarterly Journal of the Royal Meteorological Society*, *143*(704), 1685–1703. doi:
 849 10.1002/qj.3041
- 850 Huang, Siems, S., Manton, M., Protat, A., Majewski, L., & Nguyen, H. (2019). Evaluating
 851 himawari-8 cloud products using shipborne and CALIPSO observations: Cloud-top
 852 height and cloud-top temperature. *Journal of Atmospheric and Oceanic Technology*,
 853 *36*(12), 2327–2347. doi: 10.1175/JTECH-D-18-0231.1
- 854 Klepp, C. (2015). The oceanic shipboard precipitation measurement network for surface val-
 855 idation - OceanRAIN. *Atmospheric Research*, *163*, 74–90. Retrieved from [http://dx](http://dx.doi.org/10.1016/j.atmosres.2014.12.014)
 856 [.doi.org/10.1016/j.atmosres.2014.12.014](http://dx.doi.org/10.1016/j.atmosres.2014.12.014) doi: 10.1016/j.atmosres.2014.12.014
- 857 Lang, F., Huang, Y., Protat, A., Truong, S. C. H., Siems, S. T., & Manton, M. J. (2021).
 858 Shallow Convection and Precipitation over the Southern Ocean: A Case Study during
 859 the CAPRICORN 2016 Field Campaign. *Journal of Geophysical Research: Atmo-*
 860 *spheres*, 1–23. doi: 10.1029/2020jd034088
- 861 Locatelli, J. D., & Hobbs, P. V. (1974). Fall speeds and masses of solid precipita-
 862 tion particles. *Journal of Geophysical Research*, *79*(15), 2185–2197. doi: 10.1029/
 863 jc079i015p02185
- 864 Mace, G. G., Benson, S., & Hu, Y. (2020). On the Frequency of Occurrence of the Ice Phase
 865 in Supercooled Southern Ocean Low Clouds Derived From CALIPSO and CloudSat.
 866 *Geophysical Research Letters*, *47*(14), 1–8. doi: 10.1029/2020GL087554
- 867 Mace, G. G., & Protat, A. (2018a). Clouds over the Southern Ocean as observed from the
 868 R/V investigator during CAPRICORN. Part I: Cloud occurrence and phase partition-
 869 ing. *Journal of Applied Meteorology and Climatology*, *57*(8), 1783–1803. Retrieved
 870 from <https://doi.org/10.1175/JAMC-D-17-0194.1> doi: 10.1175/JAMC-D-17-0194
 871 .1
- 872 Mace, G. G., & Protat, A. (2018b). Clouds over the Southern Ocean as observed from the
 873 R/V investigator during CAPRICORN. Part II: The properties of nonprecipitating
 874 stratocumulus. *Journal of Applied Meteorology and Climatology*, *57*(8), 1805–1823.
 875 doi: 10.1175/JAMC-D-17-0195.1
- 876 Mace, G. G., Protat, A., Humphries, R. S., Alexander, S. P., McRobert, I. M., Ward,

- 877 J., ... McFarquhar, G. M. (2020). Southern Ocean Cloud Properties Derived from
 878 CAPRICORN and MARCUS Data. *Journal of Geophysical Research: Atmospheres*,
 879 1–23. doi: 10.1029/2020jd033368
- 880 McCluskey, C. S., DeMott, P. J., Ma, P. L., & Burrows, S. M. (2019). Numerical Repre-
 881 sentations of Marine Ice-Nucleating Particles in Remote Marine Environments Eval-
 882 uated Against Observations. *Geophysical Research Letters*, 46(13), 7838–7847. doi:
 883 10.1029/2018GL081861
- 884 McCluskey, C. S., Hill, T. C., Humphries, R. S., Rauker, A. M., Moreau, S., Stratton,
 885 P. G., ... DeMott, P. J. (2018). Observations of Ice Nucleating Particles Over
 886 Southern Ocean Waters. *Geophysical Research Letters*, 45(21), 11,989–11,997. doi:
 887 10.1029/2018GL079981
- 888 Mech, M., Maahn, M., Kneifel, S., Ori, D., Orlandi, E., Kollias, P., ... Crewell, S. (2020).
 889 PAMTRA 1.0: The Passive and Active Microwave radiative TRANSfer tool for sim-
 890 ulating radiometer and radar measurements of the cloudy atmosphere. *Geoscientific*
 891 *Model Development*, 13(9), 4229–4251. doi: 10.5194/gmd-13-4229-2020
- 892 Mellor, G. L., & Yamada, T. (1982). Development of a turbulence closure
 893 model for geophysical fluid problems. *Reviews of Geophysics*, 20(4), 851–
 894 875. Retrieved from [https://agupubs.onlinelibrary.wiley.com/doi/abs/10](https://agupubs.onlinelibrary.wiley.com/doi/abs/10.1029/RG020i004p00851)
 895 [.1029/RG020i004p00851](https://doi.wiley.com/10.1029/RG020i004p00851)<http://doi.wiley.com/10.1029/RG020i004p00851> doi:
 896 10.1029/RG020i004p00851
- 897 Mlawer, E. J., Taubman, S. J., Brown, P. D., Iacono, M. J., & Clough, S. A. (1997).
 898 Radiative transfer for inhomogeneous atmospheres: RRTM, a validated correlated-k
 899 model for the longwave. *Journal of Geophysical Research D: Atmospheres*, 102(14),
 900 16663–16682. doi: 10.1029/97jd00237
- 901 Muhlbauer, A., McCoy, I. L., & Wood, R. (2014). Climatology of stratocumulus cloud
 902 morphologies: Microphysical properties and radiative effects. *Atmospheric Chemistry*
 903 *and Physics*, 14(13), 6695–6716. doi: 10.5194/acp-14-6695-2014
- 904 Noh, Y. J., Miller, S. D., Heidinger, A. K., Mace, G. G., Protat, A., & Alexander, S. P.
 905 (2019). Satellite-Based Detection of Daytime Supercooled Liquid-Topped Mixed-Phase
 906 Clouds Over the Southern Ocean Using the Advanced Himawari Imager. *Journal of*
 907 *Geophysical Research: Atmospheres*, 124(5), 2677–2701. doi: 10.1029/2018JD029524
- 908 Phillips, V. T., Yano, J. I., Formenton, M., Ilotoviz, E., Kanawade, V., Kudzotsa, I., ...
 909 Tessendorf, S. A. (2017). Ice multiplication by breakup in ice-ice collisions. Part II:
 910 Numerical simulations. *Journal of the Atmospheric Sciences*, 74(9), 2789–2811. doi:
 911 10.1175/JAS-D-16-0223.1
- 912 Phillips, V. T., Yano, J. I., & Khain, A. (2017). Ice multiplication by breakup in ice-ice
 913 collisions. Part I: Theoretical formulation. *Journal of the Atmospheric Sciences*, 74(6),
 914 1705–1719. doi: 10.1175/JAS-D-16-0224.1
- 915 Raschendorfer, M. (2001). The new turbulence parameterization of LM. *COSMO Newsletter*
 916 *No. 1* (February), 89–97. Retrieved from [ThenewturbulenceparameterizationofLM](http://www.meteo.uni-stuttgart.de/~raschendorfer/thenewturbulenceparameterizationofLM)
- 917 Riehl, H., Yeh, T. C., Malkus, J. S., & la Seur, N. E. (1951, oct). The north-east trade
 918 of the Pacific Ocean. *Quarterly Journal of the Royal Meteorological Society*, 77(334),
 919 598–626. Retrieved from <http://doi.wiley.com/10.1002/qj.49707733405> doi:
 920 10.1002/qj.49707733405
- 921 Royer, P., Bizard, A., Sauvage, L., & Thobois, L. (2014). Validation protocol and inter-
 922 comparison campaigns with the R-MAN 510 aerosol lidar. *Proc. 17th International*
 923 *Symposium for the Advancement of Boundary Layer Remote Sensing* (August), 1. doi:
 924 10.13140/2.1.4778.1767
- 925 Sandu, I., & Stevens, B. (2011). On the factors modulating the stratocumulus to cumulus
 926 transitions. *Journal of the Atmospheric Sciences*, 68(9), 1865–1881. doi: 10.1175/
 927 2011JAS3614.1
- 928 Schuddeboom, A. J., & McDonald, A. J. (2021). The Southern Ocean Radiative Bias, Cloud
 929 Compensating Errors, and Equilibrium Climate Sensitivity in CMIP6 Models. *Journal*
 930 *of Geophysical Research: Atmospheres*, 126(22), 1–16. doi: 10.1029/2021JD035310
- 931 Segal, Y., & Khain, A. (2006). Dependence of droplet concentration on aerosol conditions in

- 932 different cloud types: Application to droplet concentration parameterization of aerosol
933 conditions. *Journal of Geophysical Research Atmospheres*, 111(15). doi: 10.1029/
934 2005JD006561
- 935 Seifert, A. (2008). A revised cloud microphysical parameterization for COSMO-LME.
936 COSMO News Letter No. 7, Proceedings from the 8th COSMO General Meeting in
937 Bucharest, 2006, Consortium for Small-Scale Modelling. , 25–28.
- 938 Seifert, A., & Beheng, K. D. (2006). A two-moment cloud microphysics parameterization
939 for mixed-phase clouds. Part 1: Model description. *Meteorology and Atmospheric*
940 *Physics*, 92, 45–66. doi: 10.1007/s00703-005-0112-4
- 941 Seifert, A., Blahak, U., & Buhr, R. (2014). On the analytic approximation of bulk collision
942 rates of non-spherical hydrometeors. *Geoscientific Model Development*, 7(2), 463–478.
943 doi: 10.5194/gmd-7-463-2014
- 944 Sotiropoulou, G., Vignon, E., Young, G., Morrison, H., O’Shea, S., Lachlan-Cope, T., ...
945 Nenes, A. (2020). Secondary ice production in summer clouds over the Antarctic
946 coast: an underappreciated process in atmospheric models. *Atmospheric Chemistry*
947 *and Physics*, 1–30. doi: 10.5194/acp-2020-328
- 948 Trenberth, K. E., & Fasullo, J. T. (2010). Simulation of present-day and twenty-first-
949 century energy budgets of the southern oceans. *Journal of Climate*, 23(2), 440–454.
950 doi: 10.1175/2009JCLI3152.1
- 951 Twomey, S., & Warner, J. (1967, nov). Comparison of Measurements of
952 Cloud Droplets and Cloud Nuclei. *Journal of the Atmospheric Sciences*,
953 24(6), 702–703. Retrieved from [http://journals.ametsoc.org/doi/10.1175/1520-](http://journals.ametsoc.org/doi/10.1175/1520-0469(1967)024<0702:COMOCD>2.0.CO;2)
954 [-0469\(1967\)024{\\%}3C0702:COMOCD{\\%}3E2.0.CO;2](http://journals.ametsoc.org/doi/10.1175/1520-0469(1967)024<0702:COMOCD>2.0.CO;2) doi: 10.1175/1520-0469(1967)
955 024(0702:COMOCD)2.0.CO;2
- 956 Varma, V., Morgenstern, O., Field, P., Furtado, K., Williams, J., & Hyder, P. (2020).
957 Improving the Southern Ocean cloud albedo biases in a general circulation model.
958 *Atmospheric Chemistry and Physics*, 20(13), 7741–7751. doi: 10.5194/acp-20-7741
959 -2020
- 960 Vergara-Temprado, J., Miltenberger, A. K., Furtado, K., Grosvenor, D. P., Shipway, B. J.,
961 Hill, A. A., ... Carslaw, K. S. (2018). Strong control of Southern Ocean cloud reflect-
962 ivity by ice-nucleating particles. *Proceedings of the National Academy of Sciences of*
963 *the United States of America*, 115(11), 2687–2692. doi: 10.1073/pnas.1721627115
- 964 Vignon, Alexander, S. P., DeMott, P. J., Sotiropoulou, G., Gerber, F., Hill, T. C., ... Berne,
965 A. (2021). Challenging and Improving the Simulation of Mid-Level Mixed-Phase
966 Clouds Over the High-Latitude Southern Ocean. *Journal of Geophysical Research:*
967 *Atmospheres*, 126(7), 1–21. doi: 10.1029/2020JD033490
- 968 Wood, R. (2005). Drizzle in stratiform boundary layer clouds. Part II: Microphysical aspects.
969 *Journal of the Atmospheric Sciences*, 62(9), 3034–3050. doi: 10.1175/JAS3530.1